2017

Novel Design of Nanostructured Material for Advanced Energy Conversion And Storage Devices

Wangwang Xu
Louisiana State University and Agricultural and Mechanical College, wxu26@lsu.edu

NOVEL DESIGN OF NANOSTRUCTURED MATERALS FOR ADVANCED ENERGY CONVERSION AND STORAGE DEVICES

A Thesis

Submitted to the Graduate Faculty of the
Louisiana State University and
Agricultural and Mechanical College
in partial fulfillment of the
requirements for the degree of
Master of Science

in

The Department of Mechanical & Industrial Engineering

By
Wangwang Xu
B.S., Wuhan University of Technology, 2012
M.S., Wuhan University of Technology, 2014
August 2017

ACKNOWLEDGMENTS

Firstly, I would like to express my sincere gratitude to my advisor Prof. Ying Wang for her patient and consistent guidance, encouragement, advice and experience necessary for me to work on a research topic that was of great interest to me. An undertaking of my mater program cannot be easily progressed without her supervision and instruction.

I also would like to sincerely thank Prof. Guoqiang Li, Prof. Fengyuan Lu for being willing to serve on my committee. I am very thankful to my collaborators, Dr. Liqiang Mai, Dr. Kanging Zhao and Dr. Lei Zhang at Wuhan University of technology in China; Zhiqiang Xie, Xiaodan Cui and Grant Dietrich at Louisiana State University (LSU).

I would like to acknowledge all the financial support from Research Enhancement Award (REA) and the Research Awards Program (RAP) sponsored by LaSPACE, Graduate Student Travel Award (LSU), LSU Economic Development Assistantship, ECS Travel Grant Award from the Battery Division in The Electrochemical Society.

Last but not least, I really appreciate my parents, old sister in China for their great support and love. I also would like to sincerely thank all my friends at LSU for their support and understanding in dealing with the challenges I have faced.

TABLE OF CONTENTS

LIST OF FIGURES

LIST OF ABBREVIATIONS

CV	Cyclic Voltammetry
EIS	Electrochemical impedance spectroscopy
EDS	Energy dispersive spectroscopy
FESEM	Field emission scanning electron microscopy
HRTEM	High-resolution transmission electron microscopy
PVDF	Polyvinylidene fluoride
SAED	Select area electron diffraction
SEI	Solid-electrolyte interphase
SEM	Scanning electron microscope
TEM	Transmission electron microscopy
XPS	X-ray photoelectron spectroscopy
XRD	X-ray diffraction

ABSTRACT

Nowadays, the fast-increasing energy demand for efficient, sustainable and environmentally-friendly energy storage devices remains a significant and challenging issue. Lithium ion batteries (LIBs) have been widely used as commercial energy devices in portable electronics and also shown great promise in upcoming large scale applications due to their advantages of environmental safety, efficiency in energy delivering and light weight. However, due to their limited capacity, energy densities and cycle ability, LIBs still need further improvement to expand their applications to a larger field, especially electric vehicle (EVs) and hybrid electric vehicles (HEVs), in which energy storage devices with large capacity and high energy density are urgently required. The increasing demand for their emerging applications in hybrid electric vehicles (HEVs) and electric vehicles (EVs) requires us to develop LIBs with higher energy density and power density. Significant improvements have been achieved on researching materials with high capacity to replace current commercial cathode material ($LiCoO_2$) and anode material (graphite). In this master thesis, we introduce several research works on novel design and synthesis of nanostructured electrode materials with high performance for lithium-ion batteries.

The exploration of new inexpensive rechargeable batteries with high energy-density electrodes is a key to integrate the renewable sources such as solar and wind, and address the sustainability issues. Herein, we also introduce a scalable method to prepare hierarchical graphene-encapsulated hollow SnO_2@SnS_2 nanostructures by in-situ sulfuration on the backbones of hollow SnO_2 spheres *via* a simple hydrothermal method followed by a solvothermal surface modification. The as-prepared hierarchical SnO_2@SnS_2@rGO nanocomposite can be used as anode material in lithium ion batteries, exhibiting excellent cycleability with a capacity of 583 mAh/g after 100 electrochemical cycles at a specific current

of 200 mA/g. This material shows a very low capacity fading of only 0.273% per cycle from the 2nd to the 100th cycle, lower than the capacity degradation of bare SnO_2 hollow spheres (0.830%) and single SnS_2 nanosheets (0.393%). Even after being cycled at a range of specific current varied from 2000 mA/g to 100 mA/g, hierarchical SnO_2@SnS_2@rGO nanocomposite maintains a reversible capacity of 664 mAh/g, which is much higher than single SnS_2 nanosheets (374 mAh/g) and bare SnO_2 hollow spheres (177 mAh/g). Such significantly improved electrochemical performance can be attributed to the unique hierarchical hollow structure, which not only effectively alleviates the stress resulted from the lithiation/delithiation process and maintains structural stability during cycling but also reduces aggregation and facilitates ion transportation. This work thus demonstrates the great potential of hierarchical SnO_2@SnS_2@rGO nanocomposites for application as high-performance anode material in next-generation lithium ion battery technology.

Rational design composite material is a main way to improve the performance of lithium ion batteries. Co_3O_4, attracted by the high theoretical capacity, has long suffered from low electrical transportation and dramatic large volume variations. Herein, to overcome these challenges, we report a scalable method to fabricate integrated Co_3O_4/TiO_2 composite hollow polyhedrons through a cation-exchange approach in metal-organic framework. In this synthesis, well-defined ZIF-67 particles not only serve as the host to accommodate exchanged titanium cations but also act as the template to form the hollow polyhedron structure. The obtained integrated Co_3O_4/TiO_2 composite hollow polyhedrons exhibit a high reversible capacity of 630 mAh/g at a rate of 500 mA/g after 200 cycles, accounting for 96.9% of the initial capacity, much higher than that of pure Co_3O_4 hollow polyhedrons, which can only maintain a specific capacity of 200 mAh/g and a capacity retention of only 40%. The optimized integrated

Co_3O_4/TiO_2 composite hollow polyhedrons display significant improvements in electrochemical performance, demonstrating great potential as advanced anodes in future lithium ion batteries.

CHAPTER 1. INTRODUCTION

1.1 Background

Currently, the increasing consumption of fossil fuels has resulted severely environmental problems, such as air pollution and global warming attributing to the emission of carbon dioxide and nitrous oxides. Therefore, renewable energy, such as wind energy, solar energy, geothermal energy and so on have been developed to overcome the above-mentioned challenges.[1] However, no matter on which way to obtain energy, the exploration, storage and transformation of energy needs a reasonable design.[2] Although solar energy, wind energy, geothermal energy and other non-carbon energy are clean and renewable, they are not constant and reliable sources of power. The instability of output and challenges to integrate into the grid severely limit their widespread application.[3] Energy storage technology can be employed to overcome these issues, including a set of ancillary services such as (1) frequency regulation and load following (aggregated term often used is balancing services), (2) contingency reserves, and (3) energy services that shift generation from peak to off-peak periods. In addition, it can provide services to solve more localized power quality issues and reactive power support. Overall, energy storage technology is critical to the future of renewable energy. [4-7]

According to different working mechanisms, electrochemical energy storage/conversion system can be divided into lithium-ion batteries, electrochemical capacitors (supercapacitors) and fuel cells. These three energy storage/conversion systems have three common points: 1) ions and electrons are separated. And the electrochemical reactions and the supply of energy occur between the electrodes and the electrolyte interface; (2) three main components in the systems are: cathodes, anodes, separators; (3) the two electrodes (cathode and anode) are required to have a good

conductivity.[9-12] Figure 1-1 shows kinds of current electrochemical energy storage techniques, such as fuel cells, lithium ion batteries, lead-acid batteries, Ni metal hybrid batteries, and electrolytic capacitors.[13] Among them, lithium ion batteries exhibit greater power density as well as higher energy density than the others.

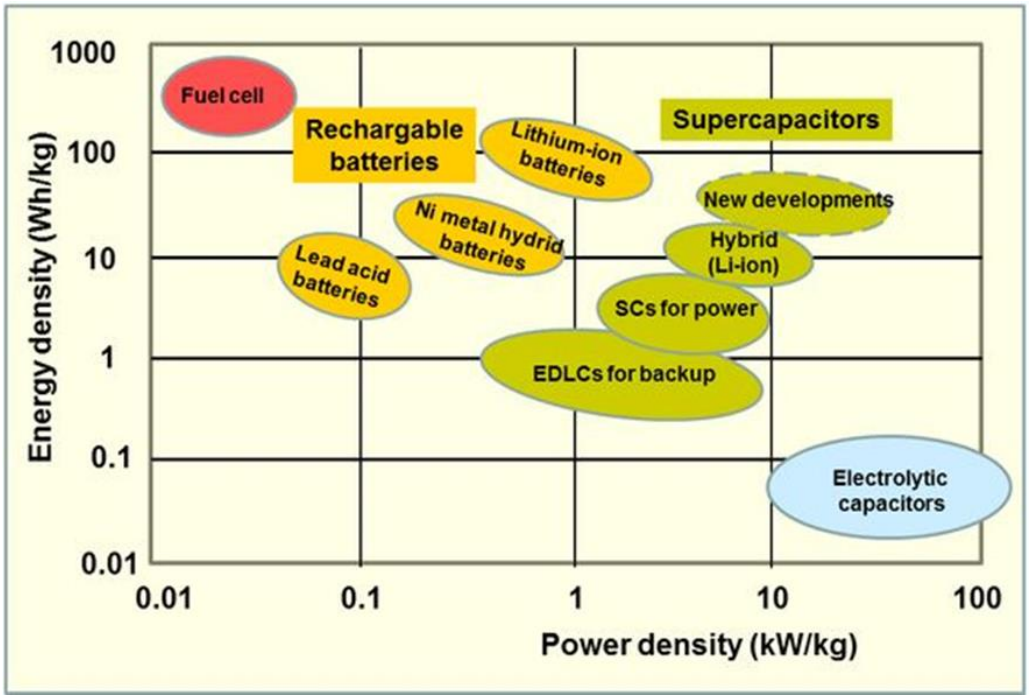

Figure 1-1 Plot of electrochemical energy storage systems [8]

Lithium ion batteries (LIBs), as the most widely used energy storage devices, have dominated the market of commercial energy storage for more than two decades due to their high energy density, long cycle life, environmental friendliness and no memory effects. In 1979, Goodenough and his co-workers first reported the use of $LiCoO_2$ as cathode material. As displayed in Figure 1-2, the intercalation of lithium ion occurs the layers of CoO_2 octahedrons. Due to the high operating voltage, high energy density, stable charge/discharge plateau, good cycle performance, $LiCoO_2$ is the most widely used commercial cathode materials. However, the main drawbacks of this

commercial cathode material are low delivery capacity of ~100 mAh/g, high price and poor conductivity, which hinder their large-scale application. [14-17]

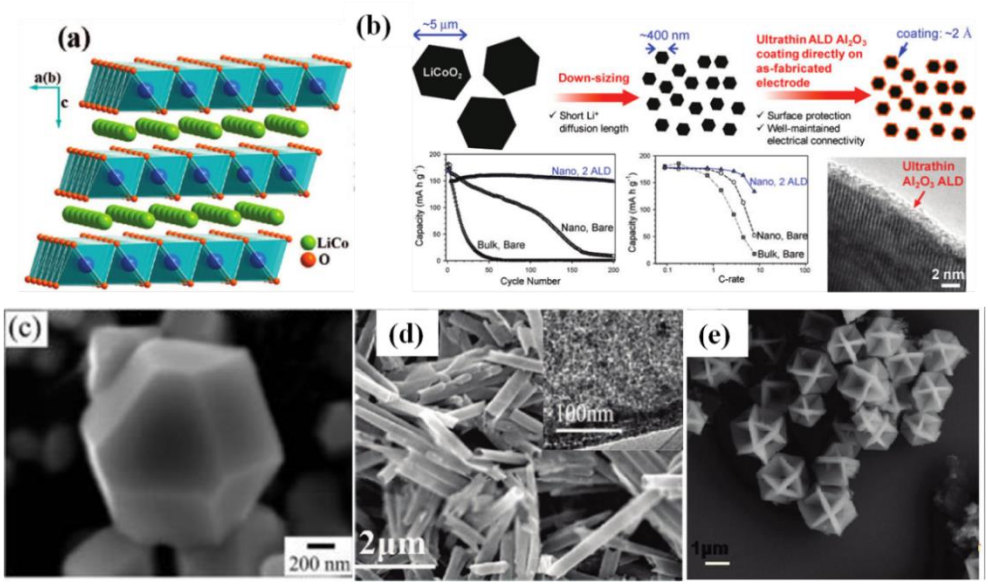

Figure 1-2 (a) Crystal structure of $LiCoO_2$; (b) the Al_2O_3-coated nanosized $LiCoO_2$ particles by ALD cycles on the bare powders; [14] (c) $LiCoO_2$ crystal with {001}, {104}, {101}, and {102} faces; [15] (d) the template prepared $LiCoO_2$ nanotubes; [16] (e) concaved cuboctahedron Li_xCoO_2 particles; [17]

Graphite materials with a layered structure have been widely used in the current commercial lithium-ion batteries due to their low price and high safety. By reversible insertion mechanism, the graphite anode can supply specific capacity of 372 mAh/g. However, due to their limited capacity, energy densities and cycle ability, LIBs still need further improvement to expand their applications to a larger field, especially electric vehicle (EVs) and hybrid electric vehicles (HEVs), in which energy storage devices with large capacity and high energy density are urgently required. Therefore, the development of new high-performance anode materials has attracted intensive research interest.[18] Base on electrochemical mechanism, anode materials can be divided into the

following three categories: alloying reaction anode materials (such as Si, SnO_2, etc.), carbon anode materials (such as graphite) and conversion reaction anode material (such as Fe_2O_3, Co_3O_4). Silicon is an attractive anode material based on alloying reaction due to the highest known theoretical charge capacity (4,200 mAh/g) and low discharge potential. [19]

1.2 The Working Mechanism of Lithium-ion Battery

Figure 1.3 displays the schematic illustration of lithium-ion battery.[20] As shown in figure 1.3, there are three main components in a lithium ion battery: cathode, anode and electrolyte. Between cathode and anode, there is a separator, which is insulative for electrons but conductive for lithium ions.[21-23] During charging process, lithium ions are extracted out from the cathode material ($Li_{1-x}CoO_2$), and inserted into the layered structure of graphite, forming Li_xC_6 compound. In discharging process, lithium ions are delithiated from the graphite and return to the positive electrode material. Electrons are moving in outside circuit, powering electronic devices. In general, in order to achieve lithium ion batteries with high power and high energy, the electrode materials should meet the following requirements: (i) large theoretical specific capacity for both cathode and anode; (ii) excellent conductivity, which supports the fast transportation of electrons in both two electrodes, ensuring the large capacity at high rate; (iii) a superior structural stability, which ensures the reversibility during charge/discharge processes and cycling life of batteries; (iv) high voltage, which is determined by the redox potential between cathode and anode, playing a key role for the energy density of battery.[24-25]

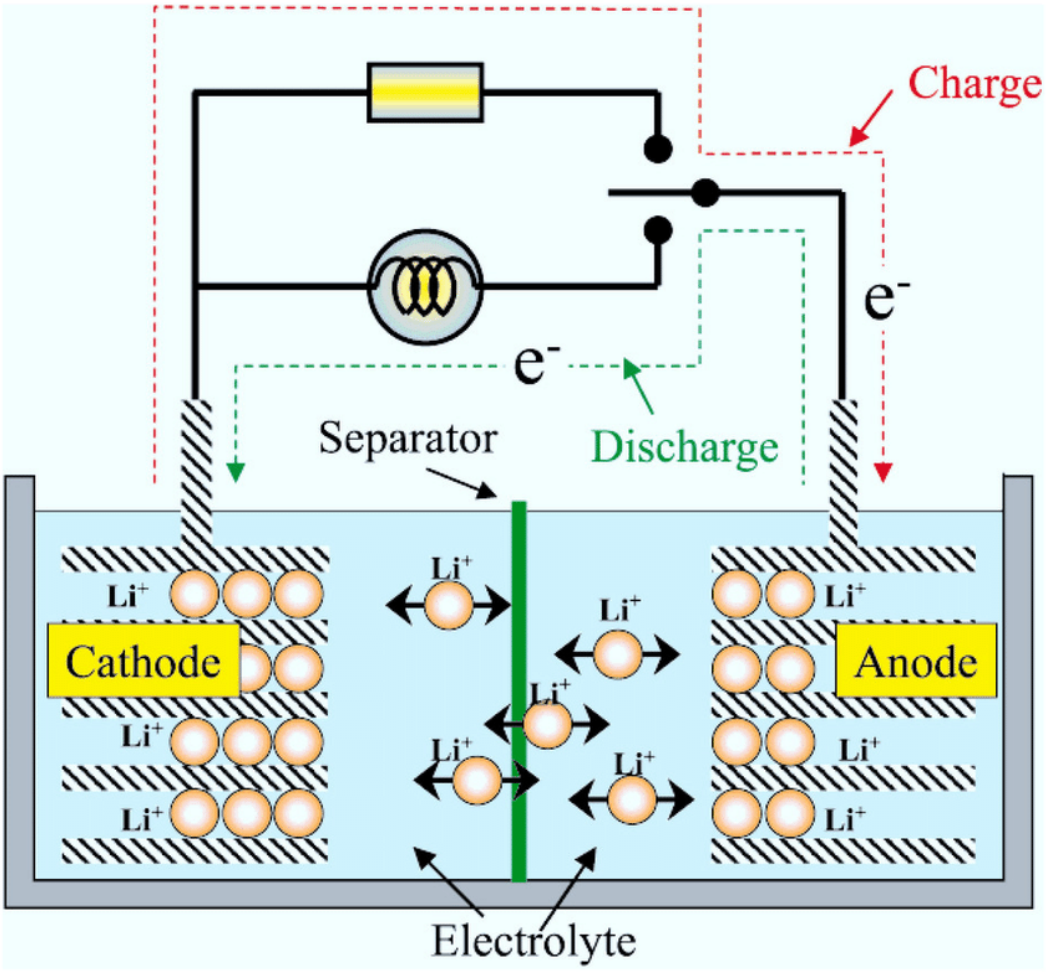

Figure 1-3 Schematic illustration of a lithium-ion battery in charging/discharging process.

1.3 Motivation and Goals

This master defense report mainly introduces three projects on development of novel cathode and anode materials with high performance for lithium ion batteries. In chapter 2, we developed a facile and scalable method to prepare two-dimensional earth-abundant jarosite-$KFe_3(SO_4)_2(OH)_6$/rGO hybrid *via* a solution-phase oxidization process at elevated temperature. In this synthesis, single-layer graphene sheets serve as both structure-directing agents and growth platforms to directly grow monocrystalline $KFe_3(SO_4)_2(OH)_6$ nanoplates with unique hexagonal shapes, forming $KFe_3(SO_4)_2(OH)_6$/rGO hybrid that exhibits a high reversible capacity of 120.5

mAh/g after 100 cycles at a specific current of 2 C and thus retains 88% of the maximum capacity. The monocrystalline jarosite- $KFe_3(SO_4)_2(OH)_6$-nanoplates/rGO hybrid exhibit a discharge capacity of 143.6, 113.9, 98.2, 83.9 and 65.9 mAh/g at 1, 2, 5, 10, and 20 C, respectively, and retain a specific capacity of 134.4 mAh/g when the specific current returns from 20 C to 1 C, displaying an excellent rate capability. At the high rate of 10 C, the jarosite- $KFe_3(SO_4)_2(OH)_6$/rGO composites maintain 70.7 mAh/g after 300 cycles with a capacity retention of 78.2%, indicating remarkable cycling stability even at a high rate. In comparison with $KFe_3(SO_4)_2(OH)_6$particles, the $KFe_3(SO_4)_2(OH)_6$/rGO nanocomposites exhibit remarkably prolonged cycling life and improved rate capability. Therefore, earth-abundant jarosite- $KFe_3(SO_4)_2(OH)_6$/rGO hybrid, demonstrates great potential for application as high-performance cathode material in new-generation lithium-ion rechargeable batteries.

The applications of alloying/dealloying materials are hindered by dramatic large volume variations and sluggish kinetics. In chapter 3, to overcome these challenges, we report a facile and scalable approach for fabricating coral-like SnO_2/C composite electrodes through a top-down strategy followed by a sol-gel method of carbon coating. In this synthesis, well-defined SnS_2 nanoflowers serve as a template to obtain monocrystalline interconnected SnO_2 nanoparticles structure, and dopamine is used as the carbon source to integrate SnO_2 nanoparticles to achieve three-dimensional coral-like SnO_2/C composite, which exhibits a high reversible capacity of 648 mAh/g after 50 electrochemical cycles and a low capacity fading of 0.778% per cycle from the 2nd to the 50th cycle, demonstrating outstanding cycling stability. Such coral-like SnO_2/C composite exhibits a discharge capacity of 1294, 784, 658, 532, and 434 mAh/g at a specific current of 100, 200, 500, 1000 and 2000 mA/g, respectively, and retains a specific capacity of 719

mAh/g when the specific current goes back to 100 mA/g, displaying an excellent rate capability. Compared to the electrodes of SnS_2 nanoflowers and interconnected SnO_2 nanoparticles, the optimized coral-like SnO_2/C composite shows significant improvements in electrochemical performance, especially in the rate capability and cycling reversibility, and thus demonstrates great potential as superior anodes in next-generation lithium ion batteries.

Complex heterostructured nanomaterials receive tremendous attention due to their superior physical and chemical performances than single-structured materials. Nevertheless, it remains a great challenge to precisely control the composition (crystalline or amorphous), size and dimension of the building blocks of hierarchical nanostructures. In chapter 4, we report a scalable method for fabricating crystalline-Co_3O_4-carbon@amorphous-FeOOH interwoven hollow polyhedrons through thermal treatment paired with solution-phase growth for application as anodes in new-generation lithium ion batteries. In this synthesis, well-defined Co_3O_4-carbon hollow polyhedrons serve as both oxidizing agent and growth platform for amorphous FeOOH nanowires. The obtained heterostructured hollow polyhedrons exhibit a high reversible capacity of 603 mAh/g after 100 cycles at the specific current of 200 mA/g, showing a capacity fading of only 0.158% per cycle between 10 to 100 cycles, much lower than that of pure Co_3O_4-carbon hollow polyhedrons (0.604%). When the specific current returns from 2000 mA/g to 50 mA/g, Co_3O_4-carbon@FeOOH heterostructure maintains a specific capacity of 1120 mAh/g, demonstrating remarkable cycleabilty and high rate capability. Such superior performance is attributed to the synergistic effect of integrated crystal and amorphous components as well as the unique interwoven heterostructure. The design of such an interwoven 3D frame architecture provides new opportunity for obtaining high-performance electrode materials in the field of energy storage.

Rational design composite material is a main way to improve the performance of lithium ion batteries. Co_3O_4, attracted by the high theoretical capacity, has long suffered from low electrical transportation and dramatic large volume variations. In chapter 5, to overcome these challenges, we report a scalable method to fabricate integrated Co_3O_4/TiO_2 composite hollow polyhedrons through a cation-exchange approach in metal-organic framework. In this synthesis, well-defined ZIF-67 particles not only serve as the host to accommodate exchanged titanium cations but also act as the template to form the hollow polyhedron structure. The obtained integrated Co_3O_4/TiO_2 composite hollow polyhedrons exhibit a high reversible capacity of 630 mAh/g at a rate of 500 mA/g after 200 cycles, accounting for 96.9% of the initial capacity, much higher than that of pure Co_3O_4 hollow polyhedrons, which can only maintain a specific capacity of 200 mAh/g and a capacity retention of only 40%. The optimized integrated Co_3O_4/TiO_2 composite hollow polyhedrons display significant improvements in electrochemical performance, demonstrating great potential as advanced anodes in future lithium ion batteries.

1.4 References

1. M. Armand, J. M. Tarascon, Nature 2008, 451, 652-657.
2. Y.H. Xu, Q. Liu, Y.J. Zhu, Y.H. Liu, A. Langrock, M.R. Zachariah, C.S. Wang, Nano Lett. 2013, 13, 470-474.
3. Z. G. Yang, J. L. Zhang, M. C. W. Kintner-Meyer, Chem. Rev. 2011, 111, 3577-3613.
4. C.N. He, S. Wu, N.Q. Zhao, C.S. Shi, E.Z. Liu, J.J. Li, ACS Nano 2013, 7, 4459-4469.
5. M. Winter, J.O. Besenhard, Electrochim. Acta 45 (1999) 31-50.
6. B. Dunn, H. Kamath, J. M. Tarascon, Science, 2011, 334, 928-935.
7. O. Mao, R.A. Dunlap, J.R. Dahn, J. Electrochem. Soc 146 (1999) 405-413.

8. H. Li, L. Shi, W. Lu, X. Huang, L. Chen, J. Electrochem. Soc 148 (2001) 915-922.

9. D. R. Rolison, L. F. Nazar, MRS Bulletin, 2011, 36, 486-493.

10. B. E. Conway, J. Electrochem. Soc. 1991,138: 1539-1548.

11. I. N. Omar, M. Daowd, O. Hegazy, G. Mulder, J. M. Timmermans, T. Coosemans, P. V.D. Bossche, J. V. Mierlo, Energies 2012, 5, 138-156.

12. A.R. Kamali, D.J. Fray, Rev Adv Mater Sci 27 (2011) 14-24.

13. D. R. Rolison, J. W. Long, J. C. Lytle, A. E. Fischer, C. P. Rhodes, T. M. McEvoy, M. E. Bourg, A. M. Lubers, Chem. Soc. Rev. 2009, 38, 226-252.

14. I. D. Scott, Y. S. Jung, A. S. Cavanagh, Y. F. Yan, A. C. Dillon, S. M. George, S. H. Lee, Nano Lett. 2011, 11, 414-418.

15. K. Teshima, S. H. Lee, Y. Mizuno, H. Inagaki, M. Hozumi, K. Kohama, K. Yubuta, T. Shishido, S. Oishi Cryst. Growth Des. 2010, 10, 4471-4475.

16. X. X. Li, F. Y. Cheng, B. Guo, J. Chen, J. Phys. Chem. B., 2005, 109, 4017-14024.

17. J. M. Tarascon, D. Guyomard, Electrochim. Acta. 1993, 38, 1221-1231.

18. C. M. Julien, A. Mauger, K. Zaghib, H. Groult, Inorganics 2014, 2, 132-154.

19. C. K. Chan, H. L. Peng, G. Liu, K. McIlwrath, X. F. Zhang, R. A. Huggins, Y. Cui, Nat. Nanotechnol. 2008, 3, 31-35.

20. G.X. Wang, B. Wang, X.L. Wang, J. Park, S.X. Dou, H. Ahn, K. Kim, J. Mater. Chem. 2009, 19, 8378-8384.

21. J.K. Hwang, S.H. Woo, J.M. Shim, C.S. Jo, K.T. Lee, J.W. Lee, ACS Nano 2013, 7, 1036-1044.

22. M. Egashira, H. Takatsuji, S. Okada, J. Yamaki, J. Power Sources 2002, 107, 56-60.

23. G. Wang, Y.Q. Ma, Z.Y. Liu, J.N. Wu, Electrochim. Acta 2012, 65, 275-279.

24. M. S. Whittingham, Chem. Rev. 2004, 104, 4271-4301.

25. Y.S. Jung, K.T. Lee, J.H. Ryu, D. Im, S.M. Oh, J. Electrochem. Soc. 2005, 152, 1452-1457.

Chapter 2. Hierarchical Graphene-Encapsulated Hollow SnO_2@SnS_2 Nanostructures with Enhanced Lithium Storage Capability

2.1 Introduction

The ever-increasing consumer market of portable electronic devices has stimulated the need for high-performance energy storage devices.[1-4] Lithium ion batteries (LIBs) as the most widely used energy storage devices, have dominated the market of commercial energy storage for more than two decades due to their high energy density, long cycle life and environmental friendliness.[5-8] To construct superior LIBs, many factors have to be taken into account, such as high energy density, large capacity with high voltage and long cycling life.[9-15] Tin and tin-based materials have been extensively studied as anodes since 1997. They are deemed as potential alternatives to replace commercial graphite anodes owing to their advantages of low voltage and high theoretical specific capacity of over 650 mAh/g, which is more than twice that of commercial graphite anode (372 mAh/g).[16-18] Unfortunately, commercialization of tin and tin-based anodes in current lithium ion batteries is limited by mechanical integrity degradation and short electrochemical cycling life of these materials, due to their large volume change up to ~250% leading to pulverization during Li-ion insertion/extraction processes.[19-20] One approach to solve this issue is to avoid conversion reaction (Sn to SnO and SnO_2) with a lower voltage limit during electrochemical cycling to maintain cycling stability. Such a method is promising, but the exploited capacity is as low as 365 mAh/g.[21]

Recently, tin or tin compound (SnO, SnO_2, SnS_2 et.al) nanostructures have been explored to alleviate their problems of fragile structure and large volume expansion during lithiation/deliation.[22-23] To overcome these drawbacks, tin-based materials with various

morphologies and structures have been obtained, including hollow spheres, nanorod arrays, nanobelts, nanosheets and nanotubes in the past years.[24-29] For example, Lou et. al prepared SnO_2 hollow spheres using a hydrothermal method according to the inside-out Ostwald ripening mechanism, which displayed an initial capacity of 1140 mAh/g and a capacity of about 700 mAh/g in the 30^{th} cycle, demonstrating much better electrochemical performance than pristine SnO_2 nanoparticles that exhibited an initial capacity of 645 mAh/g and retain almost no capacity after 20 cycles.[21] However, commersialization of tin-based electrodes is still hinderd by its severe volume change during cycling and intrinsically poor electronic conductivity. Because of its improved mechanical integrity, larger surface area, better permeabilities and more surface active sites than common nanostructures,[30-35] hierarchical nanostructure has become very appealing as electrodes in energy devices. Wang et al. synthesized ZnO-SnO_2 hiererchical nanosheets exhibiting higher photocatalytic activities for degradating methyl orange than ZnO rods or SnO_2.[36] Mai et al. prepared hierarchical $MnMoO_4$/$CoMoO_4$ heterostructured nanowires which delivered a much higher capacity and better rate capability than either constituent component.[37]

Both SnO_2 and SnS_2 are typical tin-based compounds that have been widely studied as anode materials in LIBs. Recently, SnS_2/graphene composite materials have received much attention due to their improved accomodating hosting spaces and enhanced guest accessibility for the diffusion of both Li ions and sodium ions, resulting in excellent cycling performance and rate capability.[38-41] On the contrary, SnO_2 with a higher theoretical capacity (781 mAh/g) than SnS_2 displays worse cycling stability and rate performance due ot its severe pulverization upon cycling. Therefore, it is expected that hierarchical SnO_2@SnS_2@rGO nanocomposite can be a battery electrode material with even better electrochemical performance by combining the advantages of each component.

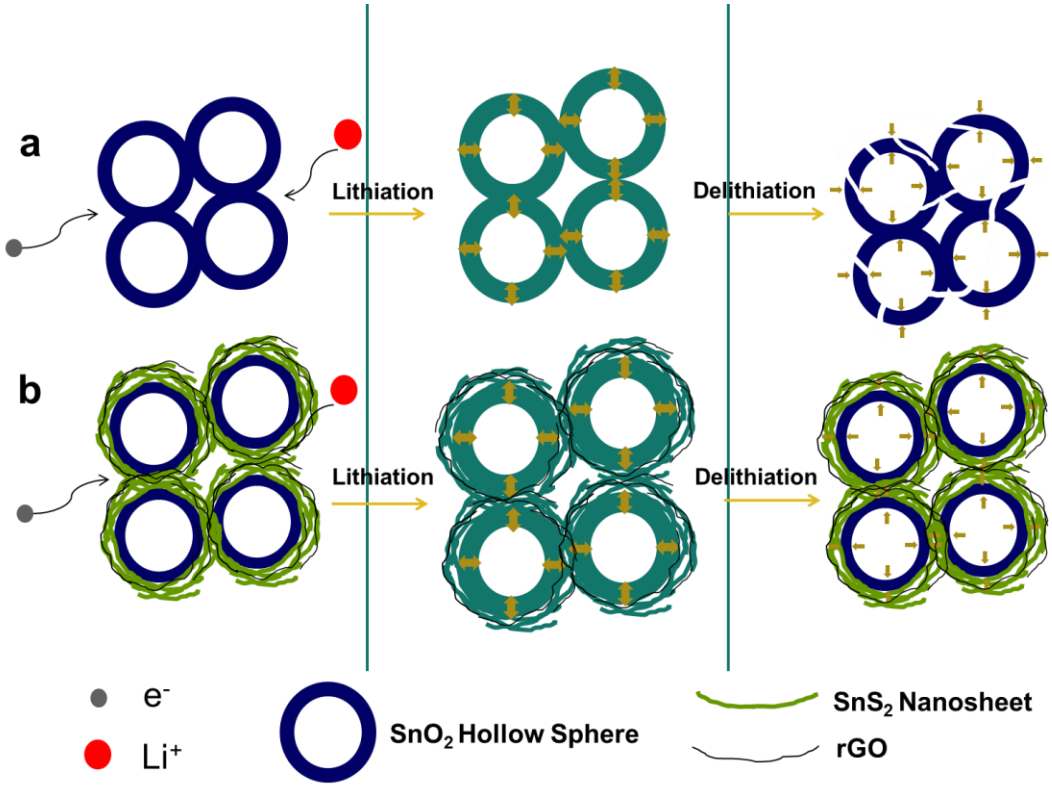

Figure 2-1 Schematic illustrations of SnO_2 hollow spheres and hierarchical SnO_2@SnS_2@rGO hollow spheres during electrochemical cycling. (a) Structural degradation of SnO_2 hollow spheres during cycling. SnO_2 hollow spheres tend to pulverize. Most of SnO_2 hollow spheres crack and crush during cycling, resulting in poor cycling performance. (b) Hierarchical SnO_2@SnS_2@rGO hollow spheres have better permeability and more surface active sites. In this structure, SnS_2 nanosheets and the shells of rGO sheets outside SnO_2 hollow spheres can improve electronic conductivity and provide facile strain relaxation during cycling, allowing them to increase in thickness without pulverization and maintaining mechanical integrity.

Herein, to combine the merits of SnO_2 hollow spheres with higher specific capacity, layered SnS_2 with better cycling stability and reduced graphene oxide (rGO) with excellent electronic conductivity, we design and synthesize hierarchical novel SnO_2@SnS_2@rGO hollowspheres via a

facile two-step growth process, for application as anodes in new-generation lithium-ion batteries. Briefly, SnO_2 hollowspheres are prepared first via a hydrothermal method. Then SnS_2 nanosheets directly grow on SnO_2 hollowspheres through facile surface sulfurization, to form a hierarchical hollow structure, which ensures mechanical integrity and electrical connection between SnO_2 hollow spheres inside and SnS_2 nanosheets and reduced graphene outside. In this structure, both SnS_2 nanosheets and reduced graphene outside serve as the protecting shells for SnO_2 hollows spheres inside from dramatic volume variation during electrochemical cycling, thus alleviate their disintegration and pulverization during lithiation/delithiation. Additionally, the inner hollow space of this structure releases stress resulted from the volume change. Compared to the fragile mechanical property of SnO_2 hollow spheres during lithiation and delithiation, hierarchical SnO_2@SnS_2 hollow spheres can effectively maintain the integrity during cycling (Figure 1). Through being encompassed with SnS_2 nanosheets, hierarchical SnO_2@SnS_2@rGO hollow spheres combine the merits of large discharge capacity and excellent cycling stability from each component, to achieve improved cycling stability with high discharge capacity. In addition, hierarchical core-shell structure provides good protection of SnO_2 hollow spheres, ensuring excellent structural stability. To improve electronic conductivity and rate capability, and further protect the shell of SnS_2 nanosheets from cracking, SnO_2@SnS_2 is futher coated with rGO. The resulted hierarchical SnO_2@SnS_2@rGO hollow spheres are expected to deliver remarkable electrochemical performance. To the best of our knowledge, such novel hierarchical electrode material is obtained for the first time. Owing to the synergic effects of each constituent in the hybrid structure, hierarchical graphene-encapsulated hollow SnO_2@SnS_2 nanostructure demonstrates great potential for application as anode material in superior lithium-ion batteries.

2.2 Experiment

Materials synthesis

All chemical reagents employed in the study were of analytical grade and used without further purification

Synthesis of SnO_2 hollowspheres

$SnCl_4$•$5H_2O$ (1.73 g) and NaOH (1.25 g) were dissolved into 30 mL distilled water under vigorously magnetic stirring for 30 min. The obtained solution was transferred into a Teflon-lined stainless autoclave (50 mL), and the heated at 200°C for 24 h. After cooling to room temperature naturaly, the resultant white powder was rinsed with deionized water and ethyl acohol repeatedly and seperated by centrifugation and dried at 60°C for 8 h.

Synthesis of SnS_2 nanosheets

$SnCl_4$•$5H_2O$ (0.54 g) and thiourea (0.49 g) were dissolved into 30 mL isopropyl alcohol under vigorously magnetic stirring for 30 min. The obtained solution was transferred into a stainless Teflon-lined autoclave and heated at 180°C for 24 h. After cooling to room temperature naturally, the resultant golden precipitate was collected by centrifugation and rinsed with deionized water and ethyl alcohol several times alternatively.

Synthesis of hierarchical SnO_2@SnS_2

The as-prepared SnO_2 (0.28 g) and 1.8 g urea were dispersed into 30 mL isopropyl alcohol by sonication for five minutes. After magnetic stirring for 30 min, the solution was transferred into a

stainless Teflon-lined autoclave (50 mL) and heated at 180°C for 36 h. After cooling to room temperature naturally, the product was collected via centrifuge and rinsed repeatly.

Synthesis of hierarchical SnO_2@SnS_2@rGO hollowspheres

The as-prepared SnO_2 (0.28 g) were dispersed into 30 mL isopropyl alcohol by sonication for five minutes. Then, 1.8 g urea and 5 ml (6 mol/L) GO (ACS Material, LLC) dispersion colloid were added into the solution. After magnetic stirring for 30 min, the solution was transferred into a stainless Teflon-lined autoclave (50 mL), heated at 180°C for 36 h. The obtained light black product was then reduced in 100 ml hydrazine hydrate solution with a concentration of 10 mmol/L for about three hours. Then the product was collected by centrifugation and rinsed with deionized water and ethyl alcohol several times alternatively. The hierarchical SnO_2@SnS_2 hollowspheres were prepared by the same method without adding GO.

2.3 Characterization

Crystallographic structures of the obtained products were determined by Rigaku MiniFlex X-ray diffraction (XRD) measurement with Cu Kα radiation in a 2θ range from 10° to 80° at room temperature. Surface morphology, particle size and energy dispersive spectroscopic (EDS) were studied using a FEI Quanta 3D FEG field emission scanning electron microscopy (FESEM). Thermogravimetric (TG) was performed on a SII STA7300 analyzer at a heating rate of 1 °C min^{-1} in air.

Electrochemical Measurements

The anodes were composed of the as-prepared tin based material (hierarchical SnO_2@SnS_2@rGO hollow spheres, or hierarchical SnO_2@SnS_2 hollow sphere, or SnO_2 hollow spheres or SnS_2

nanosheets powders) and acetylene black as well as sodium alginate binder mixed at a weight ratio of 7:2:1 in deionized water followed by drying. The anodes were assembled into CR2032-type coin cells in an argon filled glove-box using lithium foil as the cathode and celgard-2320 membrane as separator; electrolyte was 1 M $LiPF_6$ dissolved in ethylene carbonate (EC) and dimethyl carbonate (DMC) and diethylcarbonate (DEC) at a volumetric ratio of 1:1:1. The coin cells were aged for 12 h before electrochemical measurements to ensure full filtration of the electrolyte into the electrodes. Galvanostatic charge/discharge measurements were performed using an eight-channel battery analyzer (MTI Corporation) in a voltage range of 0.01-2V (versus Li^+/Li). Cyclic voltammetry (CV) measurements were performed using an electrochemical work station (CHI 6504C) over the potential range of 0.01-2.0 V vs Li^+/Li at a scanning rate of 0.1 mV/s. Electrochemical impedance spectroscopy (EIS) measurements were conducted by applying an AC potential of 5 mV amplitude in the frequency range from 0.01 to 100 kHz. Thermogravimetry (TG) was performed on a SII STA7300 analyzer at a heating rate of 1 °C/min in nitrogen.

2.4 Result and Discussion

To prepare hierarchical SnO_2@SnS_2@rGO hollow spheres, SnO_2 hollow spheres are obtained first as described in the experimental section. The formation mechanism of the SnO_2 hollow spheres can be attributed to the inside-out Owstald ripening process.[23]

$$Sn^{4+} + 6OH^- = Sn(OH)_6^{2-} \quad (1)$$

$$Sn(OH)_6^{2-} = SnO_2 + 2H_2O + 2OH^- \quad (2)$$

As shown in reaction 1 and 2, Sn^{4+} will hydrolyze to produce primary SnO_2 nanocrystals. This process is completed very quickly, therefore, these renascent solid spheres might not be well

crystallized, especially for the nanoparticles inside. Subsequently, these inner nanoparticles with higher surface energy will dissolve and further hydrolyze and condense to form SnO_2 nanocrystals on the surface of the spheres. The formation mechanism of hierarchical core shell structure has been proposed. At the initial stage of suffixation reaction in thiourea solution, H_2S that is released from the decomposition of thiourea, adsorbs on the metal surrounding SnO_2 hollow spheres. Then, S atoms interact with the metal centers and form the surface sulfur species via O↔S exchange by releasing oxygen atoms at the same time. After that, the follow-up S atoms diffuse into the lattice through analogous interstitial mechanism along oxygen vacancies, converting tin oxides into tin sulfides. Finally, the conversion reaches its limit because of the relatively lower diffusion coefficient and the diffusion depth of S atoms in the shell layer. Moreover, the sulfuration product SnS_2 tends to nucleate and grow on the reaction sites on the surface of SnO_2, because the energy of nucleation required in heterogeneous phase is generally lower than that in homogeneous phase. With the sulfuration process progressing, SnS_2 nanosheets are produced encapsulating the rest SnO_2 hollow spheres. SnO_2 hollow spheres are not only used as tin source but also as the "substrate" guiding the self-assembly growth of SnS_2 in aqueous solution without surfactant and stabilizers. Moreover, as they have typical layered structure, SnS_2 nanosheets are easily self-assembled around SnO_2 hollow spheres to form hierarchical SnO_2@SnS_2 hollow spheres. The reason that SnO_2@SnS_2 can be wrapped with graphene is clarified below. During the hydrothermal process, the outer electron orbit of Sn element can bond with the π electron cloud and the residual oxygen-containing functional groups of graphene. In addition, SnS_2 is structurally and morphologically analogous to graphene. Therefore, rGO tends to wrap around the surface of SnO_2@SnS_2 during the hydrothermal process in order to significantly reduce the high surface energy.

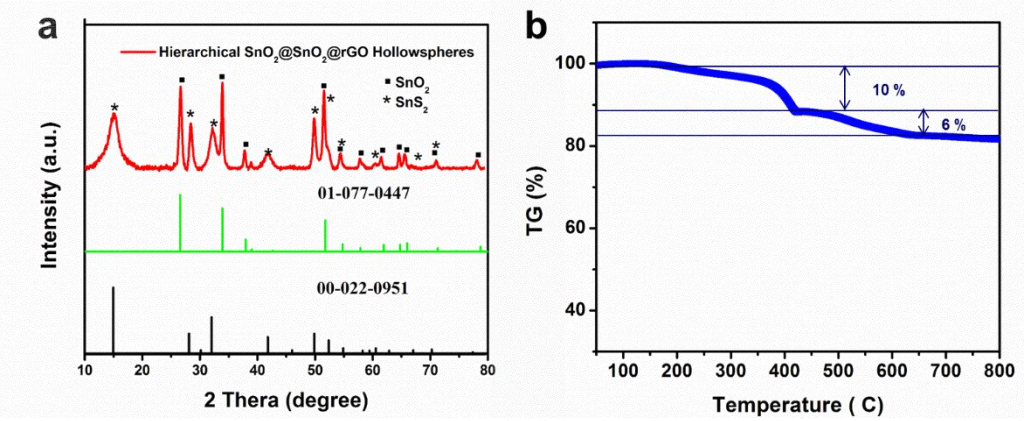

Figure 2-2 (a) XRD patterns of SnO_2@SnS_2@rGO; (b) TG analysis of SnO_2@SnS_2@rGO in air

Figure 1 compares schematic view of possible structural change of SnO_2 hollow spheres and hierarchical SnO_2@SnS_2@rGO nanostructure during repeated lithiation/delithiation processes. It can be seen that SnO_2 hollow spheres tend to crack, crush and pulverize during electrochemical cycling, resulting in structural degradation and poor cycling performance (Figure 1a). However, hierarchical SnO_2@SnS_2@rGO structure is very promising in delivering excellent electrochemical performance due to the following reasons. First, compared to the easy breaking up of bare SnO_2 hollow spheres during cycling due to their large volume variations in Figure 1a, hierarchical SnO_2@SnS_2@rGO hollow spheres, with SnO_2 hollow spheres encapsulated by SnS_2@rGO nanosheets outside, can effectively relieve the pressure resulted from the outward expansion during intercalation of lithium ions into the interior of anode materials, leading to improved mechanical integrity (Figure 1b). Second, the designed hierarchical structure with enhanced permeability, larger specific surface areas, provides more pathways for lithium ion transport, resulted in more facile and faster lithium ion transport. Meanwhile, with the rGO sheets surrounding the spheres outside, faster reaction kinetics of hierarchical SnO_2@SnS_2@rGO hollow spheres is realized.

To determine crystal structures of hierarchical SnO_2@SnS_2@rGO hollow spheres, hierarchical SnO_2@SnS_2 hollow spheres, SnO_2 hollow spheres and SnS_2 nanosheets, X-ray diffraction (XRD) measurements are conducted. Figure 2 and Figure S1 (Supporting Information (SI)) present the XRD patterns of hierarchical SnO_2@SnS_2@rGO hollow spheres and each single component, respectively. Regarding the backbones of SnO_2 hollow spheres, their XRD pattern in Figure S1a is identified as tetragonal SnO_2 with lattice parameters of a = 4.7358 Å, b = 4.7358 Å, c = 3.1851 Å, P42/mnm space group, which matches well with standard XRD pattern of tetragonal cassiterite SnO_2 (JCPDF card no. 01-077-0447). As for pristine SnS_2 nanosheets, its XRD pattern (Figure S1b) is identified as hexagonal berndtite SnS_2 (JCPDF card no. 00-022-0951) with lattice parameters of a = 3.6486 Å, b = 3.6486 Å, c = 5.8992 Å, P-3m1 space group. The XRD patterns of both hierarchical SnO_2@SnS_2 (Figure S1c) and hierarchical SnO_2@SnS_2@rGO (Figure 2a) display the crystallinity combination of bare SnO_2 hollow spheres and layered SnS_2 nanosheets, suggesting the formation of SnO_2@SnS_2 heterostructure. It is noted that there are no obvious diffraction peaks from rGO due to its low crystallinity. Then thermogravimetry (TG) measurement is performed to further investigate the content of each component in the hierarchical material. The TG curve of SnO_2@SnS_2@rGO composite in Figure 2b shows two main steps, corresponding to oxidizations of SnS_2 nanosheets and rGO, respectively. Combustion of SnS_2 nanosheets starts at around 250 ^oC and completes at approximately 425 ^oC. The calculated weight loss is 10% which is ascribed to 56 wt % SnS_2 in the sample. Combustion of rGO starts at about 500 ^oC and completed at 650 ^oC, corresponding to a 6% weight loss in the second step, and 6 wt% rGo in the sample.

Figure 3 and Figure S2 present SEM images of the as-prepared SnO_2 hollow spheres, hierarchical SnO_2@SnS_2 hollow spheres, hierarchical SnO_2@SnS_2@rGO hollow spheres and SnS_2

nanosheets. Figure 3a shows typical SEM image of the as-synthesized SnO_2 nanospheres at low magnification. Large quantities of smooth-faced SnO_2 nanospheres with diameter of about 1 m can be clearly observed. Additionally, high-magnification SEM image in Figure 3b displays a broken SnO_2 sphere, proving the as-prepared SnO_2 spheres are hollow. The hollow sphere is also shown to have an inner diameter of 400 nm with a thickness of ~300 nm. In order to obtain hierarchical SnO_2@SnS_2 hollow spheres, the as-prepared SnO_2 reacts with thiourea for 36 h. Figure 3c displays an SEM image of hierarchical SnO_2@SnS_2 hollow spheres at low magnification. It can be seen that each sphere is separated by nanosheets, indicating that aggregation of SnO_2 hollow spheres is effectively prevented by the sulfuration process. In the high-magnification SEM image, it is shown that SnO_2 hollow spheres are completely encapsulated by SnS_2 nanosheets, which directly grow on the surface of SnO_2 hollow spheres via in-situ surface sulfurization. To further study the elemental composition and distribution, EDS mapping was performed. It is clearly observed in Figure S3 that hierarchical SnO_2@SnS_2 hollow spheres consist of Sn, S and O. The EDS line scan (the inset in Figure S3) confirms that oxygen element is distributed much narrower than sulfur, indicating that oxygen element is inside and SnO_2 hollow spheres are completely encapsulated by SnS_2 nanosheets. For comparison purpose, SnS_2 nanosheets are prepared and investigated as a reference sample to compare with the performance of the composite material. Figure S2 displays SEM images of single SnS_2 nanosheets. Figure S2a shows that the as-prepared SnS_2 nanosheets are quite homogeneous, forming flower-like shapes. The magnified image (Figure S2b) reveals that SnS_2 nanosheets are about a few nanometers thick and ~2 m long. To form hierarchical SnO_2@SnS_2@rGO hollow spheres, rGO nanosheets are yielded via reduction of GO nanosheets. As shown in the SEM image at low magnification, most of the

hierarchical SnO_2@SnS_2 hollow spheres are encompassed by rGO together, forming integrated electron transportation, which can effectively improve rate capability of the sample. It can be seen from the magnified SEM image (Figure 3f) that each sphere is a surrounded completely by rGO in hierarchical SnO_2@SnS_2@rGO hollow structure. SnS_2 and rGO serve as the shell layer outside SnO_2 hollow spheres for protection. Moreover, composition of hierarchical SnO_2@SnS_2@rGO hollow structure is also determined by EDS. As seen in the EDS mapping in Figure S4, hierarchical SnO_2@SnS_2@rGO hollow spheres are composed of C, O, S and Sn, which confirms successful fabrication of this novel battery electrode material.

In order to further identity the hierarchical structure of the as-prepared samples, TEM and HR-TEM coupled with electron diffraction characterizations are carried out. As shown in Fig. 4a, SnO_2@SnS_2 core-shell structure is identified, wherein the inner hollow sphere is completely encapsulated by the surrounding nanosheets. The HR-TEM image of nanosheets in Fig. 4b exhibits lattice fringes with a spacing of 5.89, 2.95 and 2.78 Å, which can be assigned to the (001), (002) and (101) planes of SnS_2, respectively. In addition, the TEM image in Fig 4c further confirms the hierarchical structure of SnO_2@SnS_2@rGO sample. The lattice fringes with a spacing of 5.89, 3.16 and 2.78 Å are determined in the HRTEM image in Fig. 4d, corresponding to (001), (100) and (101) planes of SnS_2, respectively. Moreover, it can be clearly observed that SnS_2 nanosheets are completly coated with amorphous film, which is recognized as rGO. A selected-area electron diffraction (SAED) pattern in Fig. 4d is well indexed as a hexagonal SnS_2 phase. In addition, to evaluate the specific surface area, the N_2 adsorption-desorption measurements of all the samples are perfomed. Hierarchical SnO_2@SnS_2@rGO hollow spheres displays a Brunauer−Emmett−Teller (BET) surfaced area of 29.32 m^2/g, which is higher than that of SnO_2@SnS_2 hollow spheres (25.0 m^2/g) and bare SnO2 hollow spheres (11.9 m^2/g).

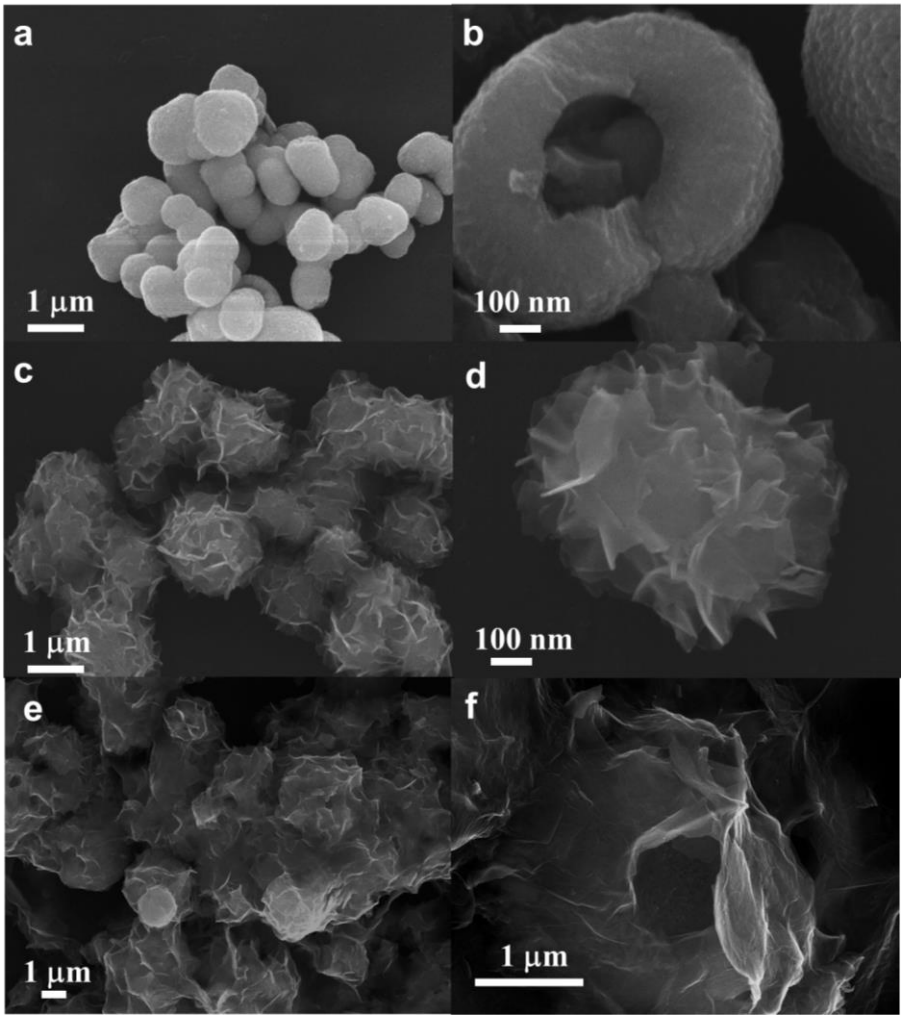

Figure 2-3 (a) SEM image and (b) magnified SEM image of SnO_2; (c) SEM image and (d) magnified SEM image of SnO_2@SnS_2; (e) SEM image and (f) magnified SEM image of SnO_2@SnS_2@rGO

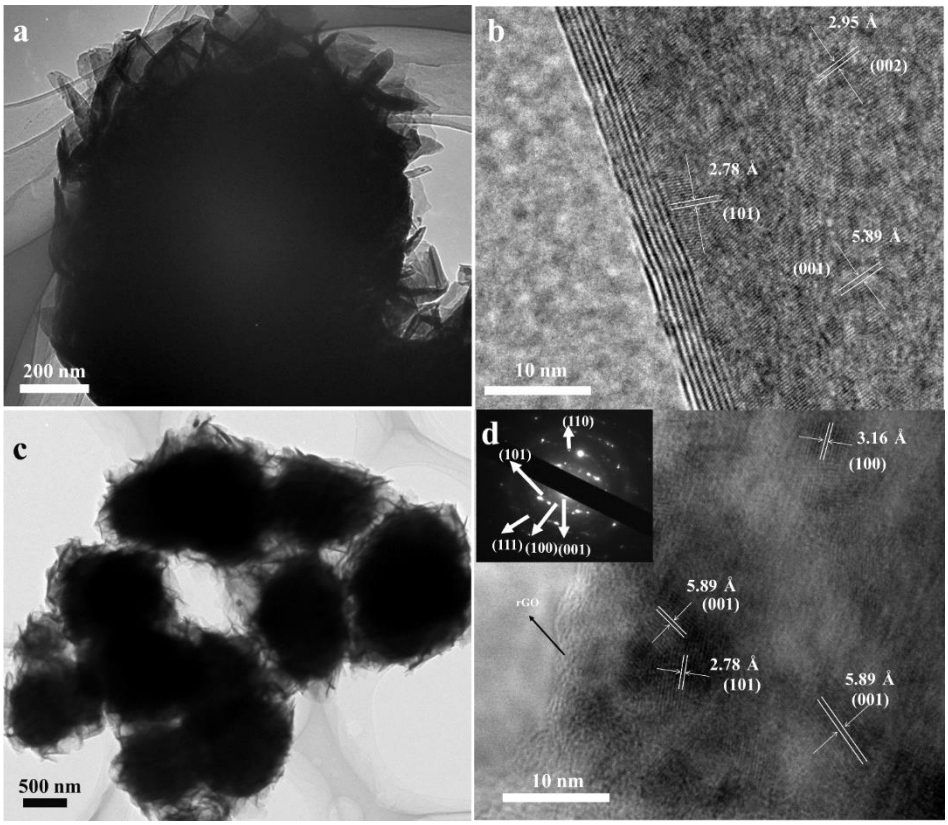

Figure 2-4 TEM image (a) and HRTEM image (b) of hierarchical SnO_2@SnS_2 hollow spheres; TEM image (c) and HRTEM image (d) of hierarchical SnO_2@SnS_2@rGO hollow spheres with corresponding SAED.

To evaluate electrochemical performances of all the samples, coin cells of hierarchical SnO_2@SnS_2@rGO hollow spheres, hierarchical SnO_2@SnS_2 hollow sphere, SnO_2 hollow spheres and SnS_2 nanosheets were assembled and cycled in a voltage range of 0.01 - 2 V (*versus* Li^+/Li). Generally, electrochemical reactions of SnO_2 and SnS_2 with lithium can be described as below:

$$SnO_2 + 4Li = 2Li_2O + Sn \quad (3)$$

$$SnS_2 + 4Li = 2Li_2S + Sn \quad (4)$$

$$Sn + xLi^+ + xe^- = Li_xSn \quad (5)$$

Reaction (3) and (4) are regarded partially reversible. Therefore, theoretical capacities of SnO_2 and SnS_2 are determined to be 782 and 650 mAh/g, respectively, based on the reaction (5).[36-37] Figure S5a displays CV curves of SnO_2 hollow spheres, showing two characteristic peaks at 0.9 and 0.1 V *vs*. Li/Li^+ in the first potential sweeping cycle, which are ascribed to decomposition of SnO_2 into metallic Sn and Li_2S (reaction 3) and generation of Li-Sn alloy (reaction 5), respectively. It is noted that the decomposition reaction is partially reversible. In subsequent cycles, intercalation of lithium ions occurs at 0.1 V and deintercalation of lithium ions occurs at 0.5 V vs. Li/Li^+, due to the alloying/dealloying reactions (reaction 5). Additional cathodic peak at 0.9 V and anodic peak at 1.3 V can be attributed to the partially reversible conversion process (reaction 3). The CV curves of SnS_2 nanosheets in Figure S5c exhibit three characteristic peaks at 1.7, 1.2 and 0.1 V in the first potential sweeping cycle, which are attributed to lithium intercalation of SnS_2 layers without phase decomposition, decomposition of SnS_2 into metallic Sn and Li_2S (reaction 4) and generation of Li-Sn alloy, respectively. In subsequent cycles, the redox peaks at 0.1 V in the anodic reaction and 0.6 V in the cathodic reaction can be ascribed to the reversible alloying and dealloying reactions of Sn and Li (reaction 5), respectively. In the CV curves of hierarchical SnO_2@SnS_2@rGO hollow spheres (Figure 5a), four broad peaks appear at the potential of 1.7, 1.2, 0.9 and 0.1 V in the first potential sweeping cycle. The peak at ~1.7 V can be attributed to lithium intercalation of SnS_2 layers without phase decomposition. The peaks around 1.2 V and 0.9 V are attributed to conversion reaction of SnO_2 (reaction 3) and SnS_2 (reaction 4), respectively. The peak at 0.1 V is related to generation of Li-Sn alloy. It can be seen that both the CV curves display characteristic peaks of SnO_2 hollow spheres and SnS_2 nanosheets, confirming the coexistence of SnO_2 and SnS_2 in the samples.

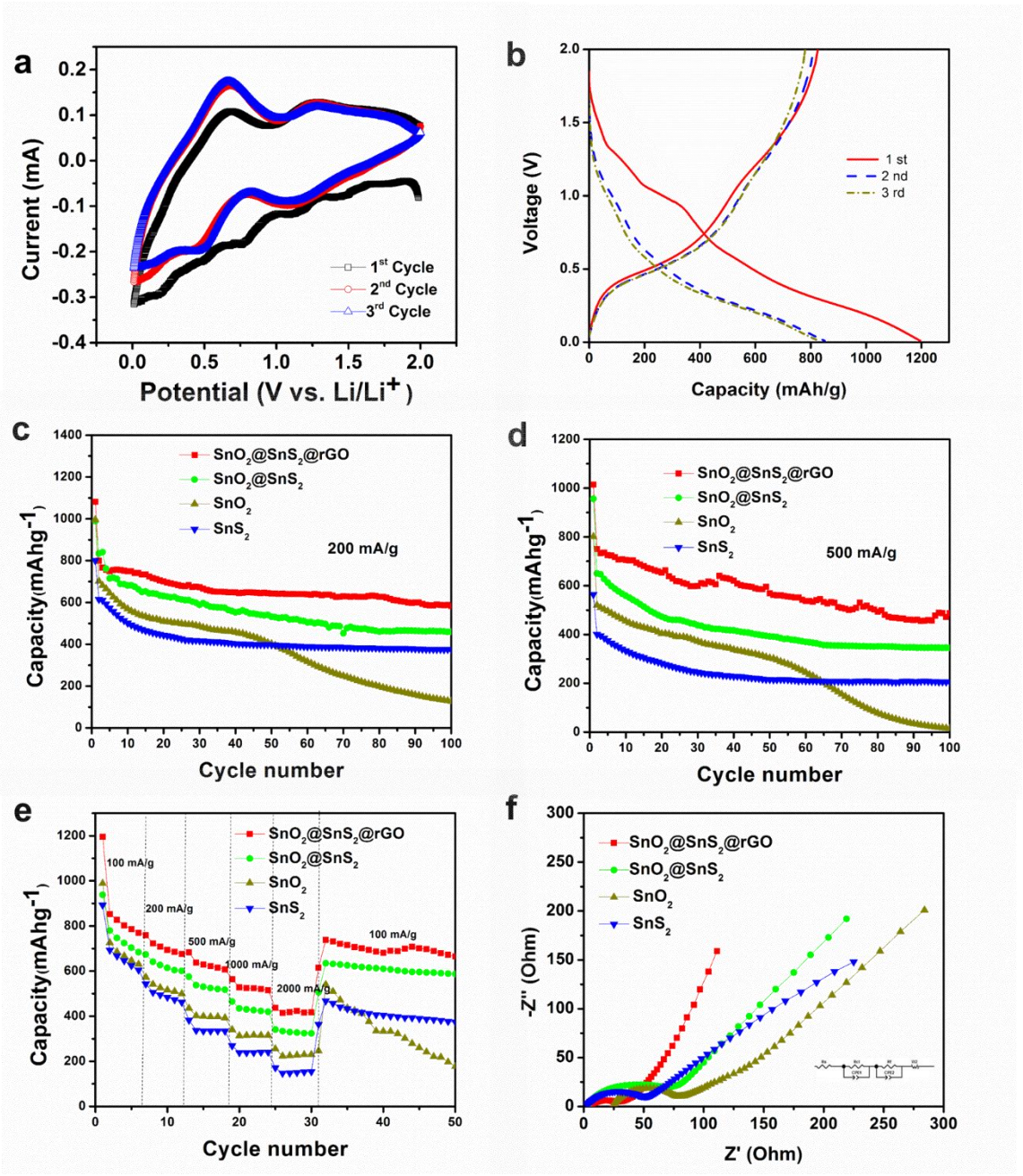

Figure 2-5 (a) CV curves and (b) galvanostatic charge-discharge profiles of the first three cycles of hierarchical SnO_2@SnS_2 hollow spheres. (c, d) Cycling performance of hierarchical SnO_2@SnS_2@rGO hollow spheres, hierarchical SnO_2@SnS_2 hollow spheres, SnO_2 hollow spheres and SnS_2 nanosheets at a specific current of 200 and 500 mAh/g, respectively. (e) Rate

performances of hierarchical SnO_2@SnS_2@rGO hollow spheres, hierarchical SnO_2@SnS_2 hollow spheres, SnO_2 hollow spheres and SnS_2 nanosheets at the specific current ranging from 100, 200, 500, 1000, 2000 to 100 mA/g; (f) Nyquist plots of hierarchical SnO_2@SnS_2@rGO hollow spheres, hierarchical SnO_2@SnS_2 hollow spheres, SnO_2 hollow spheres and SnS_2 nanosheets at 100% depth.

The charge and discharge characteristics of hierarchical SnO_2@SnS_2@rGO hollow spheres are investigated between 0.01 and 2.0 V vs. Li/Li^+ at a specific current of 100 mA/g (Figure 5b). The first discharge and charge capacities of hierarchical SnO_2@SnS_2@rGO hollow spheres are about 1195 and 826 mA h/g. The potential plateaus at 1.25 and 1.0 V are ascribed to the conversion reaction between SnO_2, SnS_2 and Li^+, leading to formation of Li_2O, Li_2S and Sn in the first discharge process. The following profiles with long slope indicate generation of Li-Sn alloy (reaction 5). Figure 5c and d summarize cycling performances of hierarchical SnO_2@SnS_2@rGO hollow spheres, hierarchical SnO_2@SnS_2 hollow spheres, SnO_2 hollow spheres and SnS_2 nanosheets. When the specific current is 200 mA/g (Figure 5c), the initial discharge capacity of hierarchical SnO_2@SnS_2@rGO hollow spheres is as high as 1150 mAh/g. However, very rapid capacity decaying is observed for all the four samples, which is generally mainly due to partial reversibility of reaction (3) and (4), generation of solid electrolyte interface (SEI) associated with decomposition of electrolyte. After 100 electrochemical cycles, hierarchical SnO_2@SnS_2@rGO sample maintains a capacity of 583 mAh/g, corresponding to a capacity fading of 0.273% per cycle from the 2^{nd} to the 100th cycles, demonstrating an outstanding cycling stability. In contrast, a drastic capacity fading is observed for pristine SnO_2 hollow spheres after 50 cycles, corresponding to a capacity fading of as high as 0.830% per cycle from the 2nd to 100th cycle. This result may be caused by expansion/contraction of SnO_2 hollow spheres during charge/discharge, leading to

severe pulverization and delamination from the conductive substrate. Meanwhile, SnS_2 nanosheets exhibit a lower initial discharge capacity at about 800 mAh/g and stable cycling performance with a capacity fading as high as 0.393% per cycle from the 2nd to the 100th cycle. These may be attributed to the low theoretical capacity of SnS_2 nanosheets and stable layered structure of SnS_2 with hosting space for swelling accommodation. In comparison with pristine SnO_2 and SnS_2 nanosheets, both hierarchical SnO_2@SnS_2 hollow spheres and hierarchical SnO_2@SnS_2@rGO hollow spheres anodes display larger discharge capacity and longer cycling life, which is attributed to unique hierarchical structure with higher permeability, reduced aggregation and better mechanical integrity. Compared to the specific discharge capacity of 450 mAh/g of hierarchical SnO_2@SnS_2 hollow structure after 100 electrochemical cycles, hierarchical SnO_2@SnS_2@rGO hollow spheres display a capacity of 583 mAh/g, showing a higher discharge capacity and capacity retention, attributing to the rGO layer wrapped outside which not only protects the inner active material from volume change during cycling, but also promotes facile electron transport and prohibits the formation of SEI film.

When the specific current is increased to 500 mA/g, enhanced cycling performance is also obtained. Compared with hierarchical SnO_2@SnS_2 hollow spheres (345 mAh/g), SnO_2 hollow spheres (15 mAh/g) and SnS_2 nanosheets (206 mAh/g) (Figure 5d), hierarchical SnO_2@SnS_2@rGO hollow spheres deliver a discharge capacity of 487 mAh/g after 100 cycles, showing the highest discharge capacity and best cycling performance. The rate performances of the as-prepared samples are summarized in Figure 5e. Hierarchical SnO_2@SnS_2@rGO hollow spheres deliver a discharge capacity of 1195, 722, 637, 527, and 436 mAh/g at a specific current of 100, 200, 500, 1000 and 2000 mA/g, respectively in Figure 5e. When the specific current goes

back to 100 mA/g, the discharge capacity is recovered to 664 mAh/g, showing the best rate capability among hierarchical SnO_2@SnS_2 (587 mAh/g), pure SnO_2 hollow spheres (177 mAh/g) and pure SnS_2 nanosheets (370 mAh/g). Hierarchical SnO_2@SnS_2@rGO hollow spheres exhibit improved rate capability due to good mechanical integrity of hierarchical structure during fast lithium intercalation and deintercalation. Moreover, rGO sheets wrapping around SnS_2 nanosheets provide a continuous pathway for fast electron transport, as confirmed by the EIS results in figure 5f. EIS technology, one of the most powerful tools for studying electrochemical kinetics, can be used to investigate the processes occurring at the electrode/electrolyte interfaces and Li^+ intercalation/de-intercalation within electrode materials in the battery cells. In the Nyquist plots, R_Ω represents the Ohmic resistance of the battery cell, including electrodes, electrolyte and other cell components. R_{ct} represents the charge transfer resistance. CPE and Z_w are the double layer capacitance and the Warburg impedance, respectively. (Figure 4f) All the Nyquist plots are composed of a depressed semicircle in the medium-frequency region followed by a slanted line in the low-frequency region. The electrode of hierarchical SnO_2@SnS_2@rGO hollow spheres shows the lowest charge transfer resistance of 30 Ω compared to hierarchical SnO_2@SnS_2@rGO hollow spheres (75 Ω), SnO_2 hollow spheres (80 Ω) and SnS_2 nanosheets (50 Ω), indicating a faster charge transfer at the electrode/electrolyte interface. Specifically, as observed in Fig. 4, the SnO_2 sample shows higher capacity but worse cycling stability than bare SnS_2. On the contrary, the SnS_2 sample exhibits relatively low capacity but much better cycling stability than SnO_2. Therefore, the SnO_2@SnS_2 composite combines the merits of both SnO_2 and SnS_2, resulting in higher capacity and better cycling stability than either component. In addition, graphene has been widely reported to effectively improve electrical conductivity of the overall electrode and can also serve as a

promising protection for the SnO_2@SnS_2 active material to restrict large volume change upon cycling. Therefore, in this work, the graphene-encapsulated hollow SnO_2@SnS_2 sample exhibits the highest specific capacity, the best cycling stability and rate capability among the four anodes (SnO_2, SnS_2, SnO_2@SnS_2, and SnO_2@SnS_2@graphene). Such significantly improved electrochemical performance can be ascribed to the synergic effect of each component in the composite. In addition, compared with most recently reported SnO_2 or SnS_2 based nanostructured anode materials, our work demonstrates significantly improved discharge capacity and prolonged sycling life even at higher specific current. For example, Guo et al [35] reported that the SnO_2@graphene composite can retain only 433 mAh/g after 20 cycles at specific current of 100 mA/g. The SnS_2 nanosheets@multiwalled carbon nanotubes composite material can maintain only 400 mAh/g after 50 cycles at specific current of 100 mA/g.[38]

In this work, the enhanced electrochemical performance of hierarchical SnO_2@SnS_2@rGO hollow spheres is mainly due to the following reasons. (1) The merits of SnO_2 hollow spheres with higher specific capacity and layered SnS_2 with better cycling stability are reveled in hierarchical SnO_2@SnS_2@rGO hollow structure. (2) In the hierarchical core-shell hollow structure, SnS_2@rGO shells stabilize the inner SnO_2 hollow spheres, which effectively alleviate the stress by local empty space to achieve an excellent structure stability and mechanical integrity. (3) The hierarchical structure provides reduced aggregation, large surface area, better permeability and more available charge storage sites, contributing to superior kinetics and excellent rate capability as well as enhanced cycling performance. Table S1 compares cycling performance of our hierarchical hollow SnO_2@SnS_2@rGO nanostructure with various SnO_2 or SnS_2 based nanostructured electrodes reported in literature[35-40], and it is found that hierarchical

SnO_2@SnS_2@rGO hollow spheres display obviously prolonged cycling life and increased specific discharge capacity as well as improved rate capability, when cycled at specific current of 200 mA/g. Therefore, such novel hierarchical SnO_2@SnS_2@rGO hollow spheres are very promising for application as superior electrode material in new-generation lithium-ion batteries, due to their easy preparation and excellent electrochemical performance.

2.5 Conclusions

In summary, hierarchical SnO_2@SnS_2@rGO hollow spheres are successfully synthesized by a facile and scalable in-situ sulfuration method which involves a simple hydrothermal treatment followed by a solvothermal process. When assembled into lithium-ion battery cells, the as-prepared material delivers a specific capacity of 583 mAh/g after 100 cycles at a specific current of 200 mA/g and a reversible capacity of 664 mAh/g after cycled at a high specific current of 2000 mA/g, demonstrating a significantly increased capacity and enhanced cycling reversibility compared to either bare SnO_2 hollow spheres or SnS_2 nanosheets. Because of their unique hierarchical hollow structure, the as-prepared hierarchical SnO_2@SnS_2@rGO hollow spheres can effectively alleviate stress and accommodate large volume change during lithiation/delithiation process, leading to excellent structural stability and mechanical integrity. This structure also provides continuous pathways for faster electron transport. Thus, cycling performance of hierarchical SnO_2@SnS_2@rGO hollow spheres is prolonged and its rate capability is greatly enhanced. Such hierarchical hollow core-shell structure can be generalized to other materials and find wide applications in high-performance energy storage devices.

Acknowledgement

This work is supported by the Research Enhancement Award (REA) and Research Awards Program (RAP) sponsored by La-SPACE. The authors also want to acknowledge the Shared Instrumentation Facility (SIF) at LSU for using XRD and SEM.

2.6 References

1. Chu, S.; Majumdar, A.; Opportunities and Challenges for a Sustainable Energy Future. *Nature*. 2012, 488, 294-303.

2. Tarascon, J. M.; Armand, M.; Issues and Challenges Facing Rechargeable Lithium Batteries. *Nature,* 2001, 414, 359-367.

3. Li, X. L.; Gu, M.; Hu, S. Y.; Kennard, R.; Yan, P. F., Chen, X. L.; Wang, C. M.; Sailor, M. J.; Zhang, J. G.; Liu, J.; Mesoporous Silicon Sponge as an Anti-pulverization Structure for High-Performance Lithium-ion Battery Anodes. *Nat. Commun.* 2014, 5.

4. Dunn, B.; Kamath, H.; Tarascon, J. M.; Electrical Energy Storage for the Grid: a Battery of Choices. *Science.* 2011, 334, 928-935.

5. Yoshino, A.; The Birth of the Lithium-Ion Battery. *Angew. Chem. Int. Ed.* 2012, 51, 5798-5800.

6. Wang, J. J.; Luo, C.; Mao, J. F.; Zhu, Y. J.; Fan, X. L.; Gao, T.; Mignerey, A. C.; Wang, C. S.; Solid-State Fabrication of SnS_2/C Nanospheres for High-Performance Sodium Ion Battery Anode, , *Appl. Mater. Interfaces*, 2015, 7, pp 11476–11481.

[7]. Zhao, K. N.; Liu, F. N.; Niu, C. J.; Xu, W. W.; Dong, Y. F.; Zhang, L.; Xie, S. M.; Yan, M. Y.; Wei, Q. L.; Zhao, D. Y.; Mai, L. Q.; Graphene Oxide Wrapped Amorphous Copper Vanadium Oxide with Enhanced Capacitive Behavior for High-Rate and Long-Life Lithium-Ion Battery Anodes." Adv. Sci. 2015.

8. Liu, N.; Lu, Z. D.; Zhao, J.; McDowell, M. T.; Lee, H. W.; Zhao, W. T.; Cui Y.; A Pomegranate -Inspired Nanoscale Design for Large-Volume-Change Lithium Battery Anodes. *Nat. Nanotechnol.* 2014, 9, 187-192.

9. Xie, Z. Q.; Ellis, S.; Xu, W. W.; Dye, D.; Zhao, J. Q.; Wang, Y.; A Novel Preparation of Core-Shell Electrode Materials via Evaporation-induced Self-Assembly of Nanoparticles for Advanced Li-ion Batteries. *Chem. Commun*. 2015, DOI: 10.1039/C5CC05577F.

10. Armand, M.; Tarascon, J. M.; Building Better Batteries. *Nature*. 2008, 451. 652-657.

11. Xie, Z. Q.; Eikhuemelo, Hillary.; Zhao, J. Q.; Cain, C.; Xu, W. W.; Wang. Y.; Ni and Fe Dual-Doped $Li_4Mn_5O_{12}$ Spinels as Cathode Materials for High-Voltage Li-ion Batteries. *J. Electrochem. Soc*. 2015, 162, A1523-A1529.

12. Bruce, P. G.; Freunberger, S. A.; Hardwick, L. J.; Tarascon, J. M.; Li-O_2 and Li-S Batteries with High Energy Storage. *Nat. Mater.* 2012, 11, 19-29.

13. Chan, C. K.; Peng, H.; Liu, G.; McIlwrath K.; Zhang, X. F.; Huggins, R. A.; Cui, Y.; High - Performance Lithium Battery Anodes Using Silicon Nanowires. *Nat. Nanotechnol.* 2008, 3, 31-35.

14. Liu, S. Y.; Lu, X.; Xie, J.; Cao, G. S.; Zhu, T. J.; Zhao, X. B.; Preferential c-Axis Orientation of Ultrathin SnS_2 Nanoplates on Graphene as High-Performance Anode for Li-Ion Batteries, , *Appl. Mater. Interfaces.* 2013, 5, pp 1588–1595.

15. Kang, B.; Ceder, G.; Battery Materials for Ultrafast Charging and Discharging. *Nature*. 2009, 458, 190-193.

16. Xie, Z. Q.; Zhao, J. Q.; Wang, Y.; One-Step Solvothermal Synthesis of Sn Nanoparticles Dispersed in Ternary Manganese-Nickel-Cobalt Carbonate as Superior Anode Materials for Lithium Ion Batteries. *Electrochim. Acta*. 2015, 174, 1023-1029

17. Lee, K. T.; Jung, Y. S.; Oh. S. M.; Synthesis of Tin-encapsulated Spherical Hollow Carbon for Anode Material in Lithium Secondary Batteries. *J. Am. Chem. Soc.* 2003, 125, 5652-5653.

18. Besenhard, J. O.; Yang, J.; Winter, M.; Will Advanced Lithium-Alloy Anodes Have a Chance in Lithium-ion Batteries? *J. Power Sources.* 1997, 68, 87-90.

19. Huang, J. Y.; Zhong, L.; Wang, C. M.; Sullivan, J. P.; Xu, W., Zhang, L. Q.; Mao, S. X.; Hudak, N. S.; Liu, X. H.; Subramanian, A.; Fan, H. Y.; Qi, L.; Kushima A.; Li, J.; In Situ Observation of the Electrochemical Lithiation of a Single SnO_2 Nanowire Electrode. *Science.* 2010, 330, 1515-1520.

20. Chen, P.; Su, Y.; Liu, H.; Wang, Y.; Interconnected Tin Disulfide Nanosheets Grown on Graphene for Li-Ion Storage and Photocatalytic Applications, *Appl. Mater. Interfaces.* 2013, 5, 12073–12082.

21. Aravindan, V.; Jinesh, K. B.; Rajiv, R. P.; Kale, V. S.; Madhavi. S.; Atomic Layer Deposited (ALD) SnO_2 Anodes with Exceptional Cycleability for Li-Ion Batteries. *Nano Energy*. 2013, 2, 720-725.

22. Zhang, L.; Zhao, K. N.; Xu, W. W.; Dong, Y. F.; Xia, R.; Liu, F. N.; He, L.; Wei, Q. L.; Yan, Y. M.; Mai. M. L.; Integrated SnO_2 Nanorod Array with Polypyrrole Coverage for High-Rate and Long-Life Lithium Batteries. *Phys. Chem. Chem. Phys.* 2015, 17, 7619-7623.

23. Liu, Z. X.; Deng, H. Q.; Mukherjee, P. P.; Evaluating Pristine and Modified SnS_2 as a Lithium-Ion Battery Anode: A First-Principles Study, *Appl. Mater. Interfaces.* 2015, 7, 4000–4009.

24. Chen, J.; Cheng, F. Y.; Combination of Lightweight Elements and Nanostructured Materials for Batteries. *Acc. Chem. Res.* 2009, 42, 713-723

25. Park, M. S.; Wang, G. X.; Kang, Y. M.; Wexler, D.; Dou, S. X.; Liu. H. K.; Preparation and Electrochemical Properties of SnO_2 Nanowires for Application in Lithium-Ion Batteries. *Angew. Chem. Int. Ed.* 2007, 119, 764-767.

26. Xu, W. W.; Zhao, K.N.; Niu, C. J.; Zhang, L.; Cai, Z. Y.; Han, C. H.; He, L.; Shen, T.; Yan, M. Y.; Qu, L. B.; Mai, L. Q.; Heterogeneous Branched Core–Shell SnO_2–PANI Nanorod Arrays with Mechanical Integrity and Three Dimentional Electron Transport for Lithium Batteries. *Nano Energy*. 2014, 8, 196-204.

27. Lou, X. W.; Wang, Y.; Yuan, C. L.; Lee, J. Y.; Archer, L. A. Template-free Synthesis of SnO_2 Hollow Nanostructures with High Lithium Storage Capacity. *Adv. Mater*. 2006, 18. 2325-2329.

28. Kim, H.; Cho, J.; Hard Templating Synthesis of Mesoporous and Nanowire SnO_2 Lithium Battery Anode Materials. *J. Mater. Chem.* 2008, 18, 771-775.

29. Wang, C.; Zhou,Y.; Ge, M. Y.; Xu, X. B.; Zhang, Z. L.; Jiang. J. Z.; Large-Scale Synthesis of SnO_2 Nanosheets with High Lithium Storage Capacity. *J. Am. Chem. Soc.* 2009, 132, 46-47.

30. Jeong, J. M.; Choi, B. G.; Lee, S. C.; Lee, K. G.; Chang, S. J.; Han,Y. K.; Lee, Y. B.; Lee, H. U.; Kwon, S.; Lee, G.; Lee, C. S.; Huh, Y. S. Hierarchical Hollow Spheres of Fe_2O_3@ Polyaniline for Lithium Ion Battery Anodes. *Adv. Mater.* 2013, 25, 6250-6255.

31. Wang, D.; Xin, H. L.; Hovden, R.; Wang, H. S.; Yu, Y. C.; Muller, D. A.; DiSalvo, F. J.; Abruña, H. D.; Structurally Ordered Intermetallic Platinum–Cobalt Core–Shell Nanoparticles with Enhanced Activity and Stability as Oxygen Reduction Electrocatalysts. *Nat. Mater.* 2013, 12, 81-87.

32. Wang, D.; Xin, H. L.; Hovden, R.; Wang, H. S.; Yu, Y. C.; Muller, D. A.; DiSalvo, F. J.; Abruña, H. D.; Structurally Ordered Intermetallic Platinum–Cobalt Core–Shell Nanoparticles with Enhanced Activity and Stability as Oxygen Reduction Electrocatalysts. *Nat. Mater.* 2013, 12, 81-87.

33. Liang, C. D.; Dudney, N. J.; Howe, J. Y.; Hierarchically Structured Sulfur/Carbon Nanocomposite Material for High-Energy Lithium Battery. *Chem. Mater.* 2009, 21, 4724-4730.

34. Sun, Y. M.; Hu, X. L.; Luo, W.; Huang, Y. H.; Self-Assembled Hierarchical MoO_2/Graphene Nanoarchitectures and Their Application as a High-Performance Anode Material for Lithium-Ion Batteries. *Acs Nano.* 2011, 5, 7100-7107.

35. Zhang, Y. C.; Zhen, N. D.; Kun, W. L.; Ming, Z.; Dionysios, D. D.; High-Performance Visible-Light-Driven SnS_2/SnO_2 Nanocomposite Photocatalyst Prepared via In situ Hydrothermal Oxidation of SnS_2 Nanoparticles, *Appl. Mater. Interfaces.* 2011, 3. 1528-1537.

36. Wang, W. W.; Zhu, Y. J.; Yang, L. X. ZnO–SnO_2 Hollow Spheres and Hierarchical Nanosheets: Hydrothermal Preparation, Formation Mechanism, and Photocatalytic Properties. *Adv. Funct. Mater.* 2007, 17, 59-64.

37. Mai, L. Q; Yang, F.; Zhao, Y. L.; Xu, X.; Xu, L.; Luo. Y. Z.; Hierarchical $MnMoO_4$/$CoMoO_4$ Heterostructured Nanowires with Enhanced Supercapacitor Performance. *Nat. Commun.* 2011, 2, 381.

38. Zhai, C. X; Du, N.; Zhang, H.; Yu, J. X.; Yang. D. R.; Multiwalled Carbon Nanotubes Anchored with SnS_2 Nanosheets as High-Performance Anode Materials of Lithium-ion Batteries. *ACS Appl. Mater. Interfaces.* 2011, 3, 4067-4074.

39. Sathish, M.; Mitani, S.; Tomai T.; Honma. I.; Ultrathin SnS_2 Nanoparticles on Graphene Nanosheets: Synthesis, Characterization, and Li-Ion Storage Applications. *J. Phys. Chem. C.* 2012. 116, 12475-12481.

40. Wu, Q.; Jiao, L. F.; Du, J.; Yang, J. Q.; Guo, L. J.; Liu Y. C., Wang Y. J.; Yuan H. T.; One-Pot Synthesis of Three-Dimensional SnS_2 Hierarchitectures as Anode Material for Lithium-Ion Batteries. *J. Power Sources.* 2013, 239, 89-93.

Chapter 3. Integrated Co_3O_4/TiO_2 Composite Hollow Polyhedrons Prepared via Cation-exchange Metal-Organic Framework for Superior Lithium-ion Batteries

3.1 Introduction

The present increasing energy demand for energy storage system with high efficiency, environmental benignity and low cost has stimulated intense research on lithium-ion batteries (LIBs).[1] Since its invention in 1991, rechargeable LIBs have gradually dominated the market of portable energy storage devices and shown great promise to satisfy the fast-increasing energy demand of a sustainable and environmentally-friendly society.[2-5] However, limited energy density and capacity of LIBs have fallen short of our expectations in expanding their applications to a broader field, especially hybrid electric vehicles (HEVs) and electric vehicle (EVs), where high energy density and large capacity are essential. [6, 7] In order to enhance the capacity and energy density of LIBs, a great deal of research has been centered on the development of novel anode materials with larger theoretical capacity, lower cost, better stability as well as durability.[8, 9]

So far, many materials have been exploited as anode materials for LIBs, such as nitrogen-doped / graphitic carbon,[10] metal oxides (MnO_2,[11] Fe_2O_3,[12] Co_3O_4,[13] NiO,[14] MoO_3,[15] SnO_2,[16, 17] TiO_2 [18]), metal sulfides (MoS_2,[19] SnS_2,[20] Co_9S_8,[21] VS_2[22]), and lithium alloys (Sn, Si, Sb)/multinary alloys.[23-25] Among them, Co_3O_4 is considered as one of the most promising anode material in LIBs due to its large theoretical capacity (890 mAh/g), which is more than two times that of current commercially used graphite anode (372 mAh/g).[26] Therefore, Co_3O_4 is expected to satisfy the future large energy-storage demand. However, accompanying

superior lithium storage capacity, Co_3O_4 also suffers from its limitations of (a) poor electronic conductivity, and (b) serious electrode pulverization, resulted from its large volume expansion/contraction during cycling. In the Li insertion and extraction process, severe volume change associated with particle crush, lead to large irreversible capacity loss and poor capacity retention, hindering Co_3O_4-based anodes from commercial applications. Over the years, extensive efforts have been focused on addressing the first issue of poor electronic conductivity, via fabricating nanostructures hybridized with conducting materials, including amorphous carbon, graphene oxide nanosheet and conductive polymers, in an attempt to improve electronic conductivity and structure stability of Co_3O_4. For example, as reported by Lin et al., peapod-like Co_3O_4@Carbon nanocomposites can supply the specific capacity of as high as 1050 mAh/g, which is much higher than that of single Co_3O_4 nanoparticles (372 mAh/g) after 50 cycles at specific current of 1 C.[27] Moreover, Co_3O_4@Carbon nanotube arrays, reported by Schth et al., can provide the specific capacity of 700 mAh/g at 10 mA/g after 100 cycles, which is far more than that of the singe mesoporous Co_3O_4 (199 mAh/g).[28] Their work makes great progress on improving the conductivity of Co_3O_4 and its structural stability to a certain extent. However, insufficient emphasis has been placed on overcoming the second challenge-severe volume change during lithiation and delithiation due to volume expansion of inner Co_3O_4, which causes the protective coating layer to crack and fracture, rendering the original core–shell structure. The volume change associated with particle crush leads to large irreversible capacity loss and poor capacity retention, hindering commercial applications of Co_3O_4-based anodes.

Another transition metal oxide, TiO_2, more specifically, anatase-TiO_2, has received increasing attention as novel anode material for LIBs due to its low cost, good cycling stability as well as

environmental friendly quality.[29] In comparison with most transition metal oxides, anatase-TiO_2 displays better cycling ability because of its relatively low theoretical capacity (178 mAh/g) and fewer inserted amount of lithium ions. Moreover, due to its excellent structural stability, TiO_2 can also act as a promising protective layer for active material to maintain mechanical integration during cycling. For example, Cui et al. designed sulphur-TiO_2 yolk-shell nanoarchitecture.[30] The sulphur-TiO_2 yolk-shell nanoarchitecture displays an initial capacity of 1030 mAh/g at 0.5 *C* and a capacity decay as small as 0.033% per cycle after 1000 cycles, presenting superior cycling ability. Such remarkable performance is attributed to the stable TiO_2 shell and novel yolk-shell nanoarchitecture. Moreover, as reported in previous reports, in comparison with pure TiO_2 and transition metal oxides, TiO_2/transition metal oxides composites exhibit enhanced electrochemical performances due to the positive synergistic effect**.** [31-33] The electrochemical performance of the composite with different ratio of TiO_2 and transition metal has also been explored. [31-35] The composite with a higher mass content of TiO_2 usually exhibits a relative lower initial capacity with better cyclability. For example, Liu et al. reported that Co_3O_4/TiO_2 composite with a mass ratio of 6:1, exhibits limited improved cyclability over 150 cycles compared to pure Co_3O_4.[32] Moreover, Jaumann et al. reported the CoO/TiO_2 composite with a very high TiO_2 content (>50%) that shows excellent cycle ability but very low capacity. [35] In this respect, the strategy of designing composite nanoarchitecture with stable TiO_2 and large-capacity metal oxides can help one realize synergic property of electrochemistry.

Metal-organic frameworks (MOFs), composed by metal clusters with electron-donating organic ligands, have been intensively studied as a result of their versatile structural topologies, tunable functionalities, as well as wide applications in catalysis, gas storage, and biomedical imaging. In

recent years, cation exchange has emerged as an effective synthetic route to the modification of secondary building units of MOFs.[36] According to Ringwood's rule [37], ions with similar electronegativity could replace each other. The ions with the lower electronegativity will be exchanged more easily because it can form stronger bonds with the one with larger ionic character. Recently, it has been widely used to improve chemical/physical properties of molecules and nanocrystals, expanding the applications of MOFs. For example, Rosi et al., reported that their CO_2 adsorption properties can be tuned by cation exchange. Because the pore size of MOF-1 can be synthetically modified *via* straightforward cation-exchange experiments, such modifications can be used to tune the CO_2 adsorption capacity of MOF-1.[38] Moreover, the cation exchange process can also be used to synthesize composite heterostructures. Hollingsworth et.al have synthesized PbSe/CdSe core/shell quantum dots using a controllable partial cation exchange method. The resulted core/shell nanocrystal quantum dots are stable against fading and spectral shifting due to the synergic physical properties.[39]

Herein, we report for the first time, the controllable design of Co_3O_4/TiO_2 composite hollow polyhedron nanoarchitecture *via* cation exchange in zeolitic imidazolate frameworks (ZIF-67), followed by thermal treatment. Co^{2+} cation can be replaced by Ti^{4+} cation more easily than Co^{3+} due to its lower electronegativity. The Co_3O_4/TiO_2 composite hollow polyhedrons display prolonged and stable cycling for over 200 cycles as anode material for LIBs. The unique advantage of such composite hollow polyhedrons lies in the synergistic effect of two integrated components as anode material for LIBs. Specifically, Co_3O_4 can supply durable large capacity at high specific current, due to the integration of TiO_2 with stable structure and higher conductivity. Moreover, the internal void space can effectively accommodate large volumetric expansion of Co_3O_4 during

cycling, maintaining structural integrity of the shell. In addition, owing to better conductivity, the TiO_2 component provides faster pathways for electron transportation, improving electrochemical reaction kinetics of the composite. In comparison with bare Co_3O_4 hollow polyhedrons, the composite nanostructures are found to exhibit superior capacity retention and rate capability. At a specific current of 500 mA/g, the composite nanostructures provide an initial capacity as high as 662 mAh/g, and maintain a stable capacity of 642 mAh/g after 200 cycles, accounting for 96.9% of the initial capacity, much higher than pure Co_3O_4 hollow polyhedrons that can only maintain a specific capacity of 200 mAh/g and a capacity retention of only 40%. To the best of our knowledge, this is the first time that Co_3O_4 with this level of performance has been reported for application as LIB anode material.

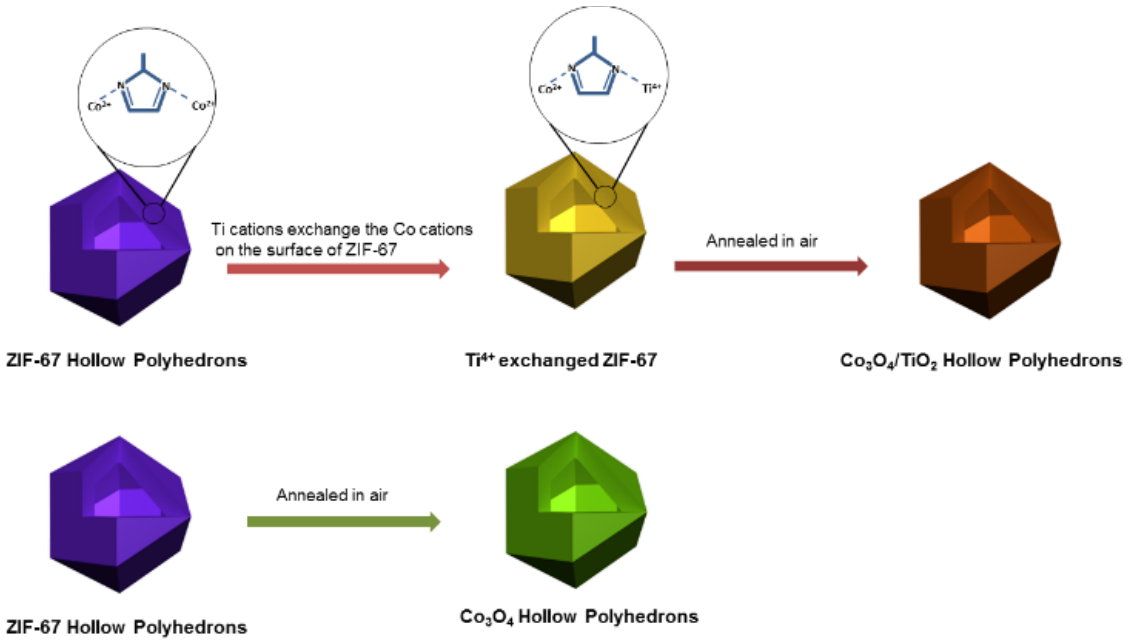

Figure 3-1 The ZIF-67 sample possesses a hollow polyhedron structure. After cation exchange with Ti^{4+}, ZIF-67 is converted into Ti^{4+}/Co^{2+} composite ZIF-67. Then Co_3O_4/TiO_2 composite

hollow polyhedrons are obtained after thermal annealing in air. For comparison purpose, pure Co_3O_4 hollow polyhedrons are obtained without cation exchange.

3.2 Experimental Section

Synthesis of ZIF-67: In a typical synthesis, 2-methylimidazole (1.97 g) was dissolved in a mixed solution of 20 ml methanol and 20 ml ethanol. $Co(NO_3)_2 \cdot 6H_2O$ (1.746 g) was dissolved in another mixed solution of 20 ml methanol and 20 ml ethanol. The above two solutions were then mixed under continuous stirring for 10 minutes, and the final solution was kept for 20 hours at room temperature.[40] The resulted purple precipitate was collected by centrifugation, washed in ethanol several times, and dried at 80 °C.

Synthesis of Composite Co_3O_4/TiO_2 Hollow Polyhedrons via Cation-exchange: Tetrabutyl titanate (6 mmol) was dissolved in 100 mL dry deaerated DMF. After being stirred for 10 mins, 100 mg ZIF-67 was added in the solution. The suspensions were stirred gently for 48 hours at room temperature (25 °C). After the exchange of Ti^{4+} cations, the precipitates were collected by centrifuge and rinsed with DMF and alcohol several times, and dried at 80 °C for 12 h. Finally, the product was obtained by annealing the powder at 300 °C with a heating rate of 2 °C/min and kept at that temperature for 2 h.

Synthesis of Co_3O_4 Hollow Polyhedrons: The ZIF-67 polyhedrons were dispersed in a crucible, heated to 300 °C with the heating rate of 2 °C/min and kept at that temperature for 2 h in the furnace. After that, the furnace is cooled down to room temperature naturally.

*Characterization:*The chemical states of obtained products were studied by X-ray photoelectron spectroscopy (XPS). XPS data were collected on an AXIS165 spectrometer using a twin-anode Al

Kα (1486.6 eV) X-ray as the excitation source with the charge neutralization function being turned on. Crystallographic structure were determined by Rigaku MiniFlex X-ray diffraction (XRD) measurement with Cu Kα radiation(λ = 1.5405 Å) in a 2θ range from 10° to 90° with scanning rate of 1 °/min. Energy dispersive spectroscopic (EDS) as well as sample morphology were characterized by a FEI Quanta 3D FEG field emission scanning electron microscopy (FESEM) and a JEM-1400 transmission electron microscope (TEM).

Electrochemical Measurements: The working electrode was prepared by casting a mixture consisting of as-prepared Co_3O_4/TiO_2 composite hollow polyhedrons, or pure Co_3O_4 hollow polyhedrons, carbon black and sodium alginate binder mixed at a weight ratio of 7:2:1 in deionized water onto a copper foil with a doctor blade, followed by drying at 70 °C. CR2032-type coin cells were assembled in an argon filled glove-box, using lithium foil as the counter electrode, Celgard-2320 membrane as the separator, and 1 M LiPF6 dissolved in dimethyl carbonate (DMC)/ethylene carbonate (EC)/diethylcarbonate (DEC) at a volumetric ratio of 1:1:1 as the electrolyte, then followed by 12h aging treatment before electrochemical measurements. Galvanostatic charge/discharge experiment were carried out on an eight-channel battery analyzer (MTI Corporation) between 0.01V and 3.00 V versus Li^+/Li. Cyclic voltammetry (CV) measurements were conducted on an electrochemical work station (CHI 6504C) over the potential range of 0.01 - 3.00 V vs. Li^+/Li at 0.1 mV/s scanning rate. Electrochemical impedance spectroscopy (EIS) measurements were operated by applying an AC potential of 5 mV amplitude in the frequency range from 0.01 to 100 kHz.

3.3 Result and Discussion

Synthesis and Characterization of the Co_3O_4/TiO_2 composite hollow polyhedrons

The fabrication procedure of Co_3O_4/TiO_2 composite hollow polyhedrons is illustrated in Figure 1. The ZIF-67 hollow polyhedrons were prepared by a precipitation method with the precursors of cobalt nitrite and 2-methylimidazole in methanol for 20 hours at room temperature. Then, cation exchange took place on the surface of ZIF-67 in the solvent of dimethyl formamide. Ti^{4+} has much lower electronegativity than that of Co^{2+}. Therefore, it is remarkable that they can undergo the cation exchange,[36] which is described in the following steps. First, when ZIF-67 hollow polyhedrons are completely surrounded by the solvent of dimethyl formamide, the inorganic clusters of ZIF-67, also called secondary-building units, will be partially solvated. Then, the bond between the cluster and Co^{2+} cations starts to break, and gradually bound with Ti^{4+} cations. In this process, the solvent molecules step-wisely connect to Co^{2+} cations as they remain partially bound to the cluster. Next, Ti^{4+} cations partially replace Co^{2+} cations in the secondary building units, forming Ti^{4+}-exchanged ZIF-67.[12] Finally, the composite Co_3O_4/TiO_2 hollow polyhedrons are yielded through decomposition and oxidization of Ti^{4+} exchanged ZIF-67 via sintering in air for two hours. For comparison purpose, pure Co_3O_4 hollow polyhedrons are synthesized by annealing ZIF-67 directly.

In order to examine the stability of Ti^{4+} exchanged ZIF-67, crystal structure of the products formed at each step is determined by XRD, as shown in Figure S1. Figure S1 displays XRD pattern of ZIF-67 and Ti^{4+} exchanged ZIF-67 hollow polyhedrons. It is found that all the typical diffraction peaks from (011), (002), (112) and (222) planes, are consistent with previous reports.[40] Moreover, the Ti^{4+} exchanged ZIF 67 displays the same peak positions as those from ZIF-67, indicating that ZIF 67 is stable and flexible enough to accommodate the exchanging Ti^{4+} cations. To confirm the Ti^{4+} cations exchanged in ZIF-67, XPS studies were carried out and the results are shown in Figure

2a and S2. Figure 2a displays the survey scan spectra of ZIF 67 and Ti^{4+} exchanged ZIF 67. The XPS spectrum of ZIF-67 from XPS analysis exhibits the principal C1s, O1s, N1s and $Co2p_{3/2}$ core levels, with no impurities. After exchanging with Ti^{4+} cations, the XPS spectrum of Ti^{4+} exchanged ZIF-67 reveals the addition of Ti $p_{3/2}$ peak, confirming successful exchanging of Ti^{4+} cations in ZIF-67. Detailed scans of the Co 2p range and Ti 2p range are illustrated in Figure S2a and S2b respectively. In the Co 2p XPS spectra, the Co $2p_{3/2}$ and Co $2p_{1/2}$ components are distinct along with two satellite peaks. The Co $2p_{3/2}$ and Co $2p_{1/2}$ peaks, located at binding energies of 780.5 and 795.4 eV, respectively, are characteristic of Co^{2+} species. In the Ti 2p spectra, there are two peaks, Ti 2p3/2 and Ti 2p1/2, centering at 457.9 and 463.7 eV respectively, in accordance with Ti^{4+} species.

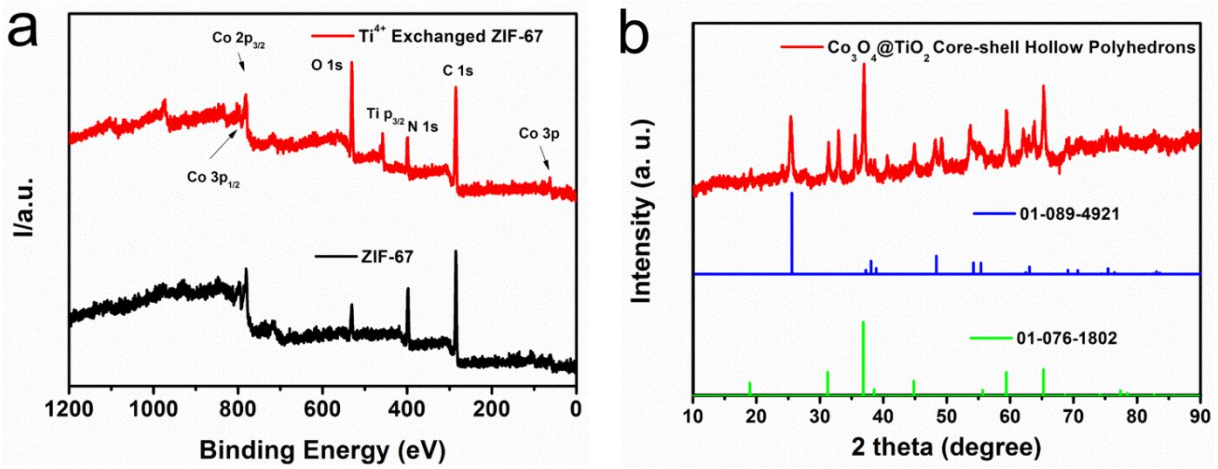

Figure 3-2 (a) XPS survey spectrum of ZIF-67 and Ti^{4+} exchanged ZIF-67 hollow polyhedrons. (b) XRD patterns of Co_3O_4/TiO_2 composite hollow polyhedrons.

The crystal structures of Co_3O_4 hollow polyhedrons and Co_3O_4/TiO_2 composite hollow polyhedrons are also determined by XRD, as shown in Figure 2b. After sintering in air, XRD analysis indicates ZIF-67 hollow polyhedrons are completely converted into Co_3O_4 hollow polyhedrons, as displayed in Figure 2b. Co_3O_4 hollow polyhedrons are identified as cubic cobalt

oxide with lattice parameters a = b = c = 8.056 Å, Fd-3m space group, which is in good agreement with standard XRD patterns of cubic Co_3O_4 (JCPDF card no.03-065-3103).[41] As for the Co_3O_4/TiO_2 composite hollow polyhedrons, their XRD pattern displays mixture of cubic Co_3O_4 and anatase TiO_2. The as-formed TiO_2 is identified as cubic anatase TiO_2, with lattice parameters of a = 3.6486 Å, b = 3.6486 Å, c = 5.8992 Å, which match well with those of standard XRD patterns of cubic anatase TiO_2 (JCPDF card no. 01-076-1802).[42] The co-existence of cubic Co_3O_4 and anatase TiO_2 confirms the formation of Co_3O_4/TiO_2 composite structure.

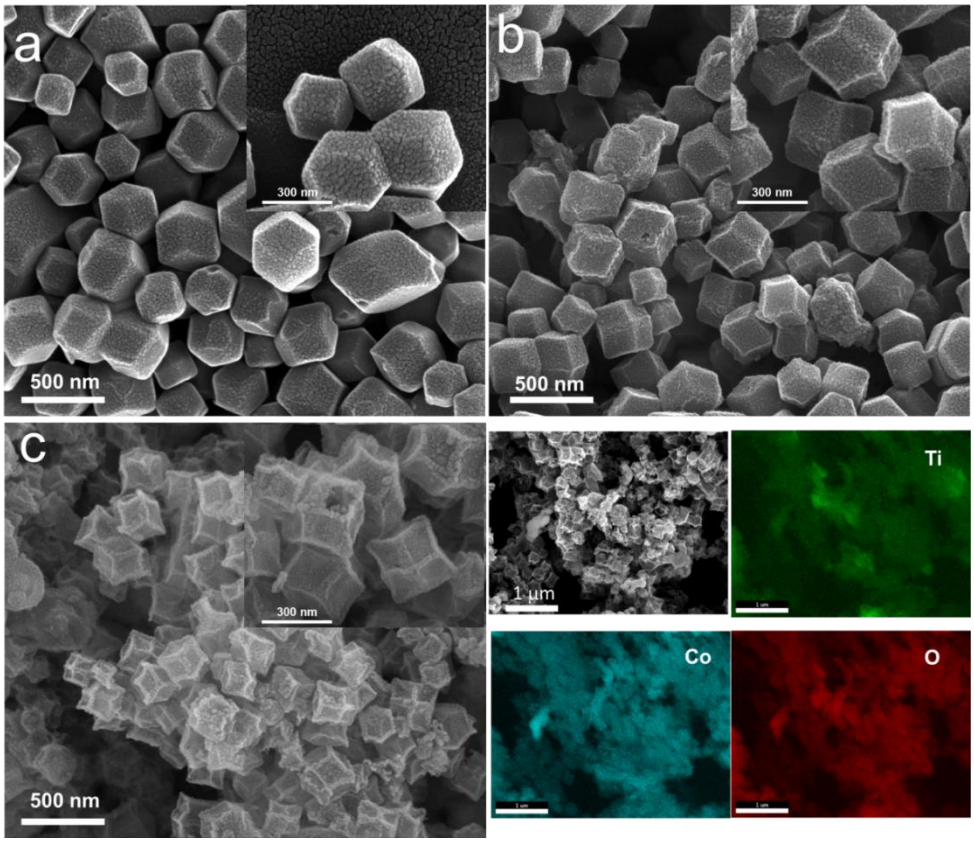

Figure 3-3 SEM images of (a) ZIF-67 hollow polyhedrons, (b) Ti^{4+} exchanged ZIF-67 hollow polyhedrons, (c) Co_3O_4/TiO_2 composite hollow polyhedrons, (d) SEM image of Co_3O_4/TiO_2 composite hollow polyhedrons and corresponding EDS mappings of O, N, C and Sn elements.

In order to investigate the morphology of the products in each step, their FESEM images have been taken and displayed in Figure 3. Figure 3a manifest the SEM image of the well-defined ZIF-67 hollow polyhedrons. In Figure 3a, the size and polyhedral shape of ZIF-67 nanoparticles are quite uniform. As can be seen in the inset magnified SEM image in Figure 3a, ZIF-67 hollow polyhedrons are about 200 nm in width. As displayed clearly in Figure 3b, the size and polyhedral shape of ZIF-67 nanoparticles are retained well after the cation exchange with Ti^{4+} for about two days, except that the surface of the polyhedrons becomes slightly rougher. To explore the influence of the concentration of titanium source, the cation-exchange process was also taken in a tetrabutyl titanate concentration as high as 12 M. As seen in Figure S3, the polyhedral shape of the sample is maintained at a high concentration of titanium source, indicating that ZIF-67 particles are stable enough to accommodate the inserted titanium cations. After thermal treatment, the Co_3O_4/TiO_2 composite is obtained with the retained hollow-polyhedron shape, as displayed in Figure 3c. Also in Figure 3c, many tiny nanoparticles are observed on the rough surface. Moreover, in Figure 3d, some broken polyhedral particles display open voids, indicating well maintained hollow structures of ZIF-67. It can be seen that the Co_3O_4/TiO_2 composite hollow polyhedrons, with a thickness of about 20 nm, are composed of closely interconnected nanoparticles. The composition of Co_3O_4/TiO_2 composite hollow polyhedrons is also confirmed by EDS mapping. EDS of the elemental mappings is performed on the sample of Co_3O_4/TiO_2 composite hollow polyhedrons and the results are shown in Figure 3d, S4. The cobalt, titanium, and oxygen signals overlap uniformly across the entire sample, indicating uniform formation of Co_3O_4/TiO_2 composite hollow polyhedrons. The mass ratio of Co_3O_4 and TiO_2 is about 8:2. The corresponding SEM image, EDS,

and XRD pattern clearly demonstrate the morphology and structure of Co_3O_4/TiO_2 composite hollow polyhedrons.

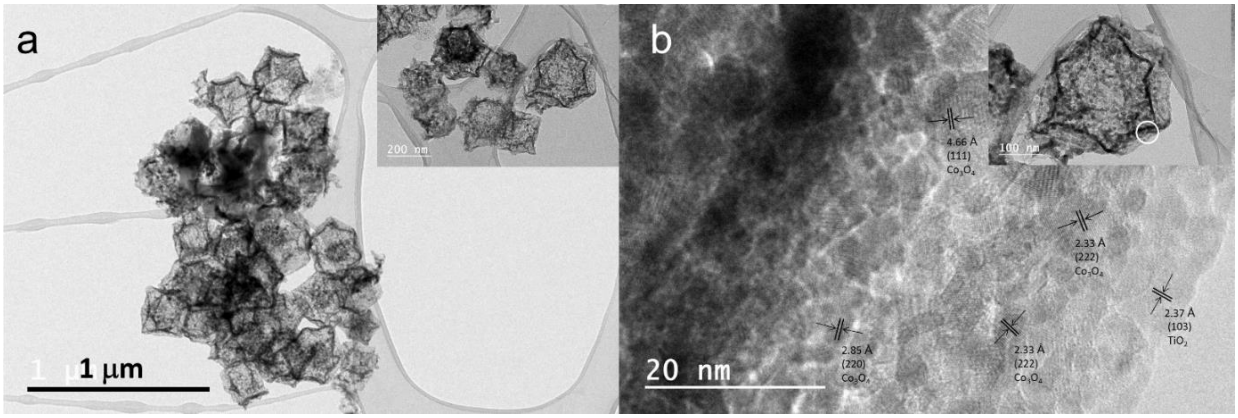

Figure 3-4 (a) The TEM image and (b) HRTEM image of Co_3O_4/TiO_2 composite hollow polyhedrons.

In order to further identify the microstructure and crystallographic relationship of TiO_2 and Co_3O_4, TEM and HRTEM imaging are carried out on the samples. The TEM images of Co_3O_4/TiO_2 composite hollow polyhedrons in Figure 4a reveal their microstructure, confirming the uniform polyhedral morphology and the inner void of the composite hollow polyhedrons. To explore more details of the sample, Figure 4b presents the corresponding HRTEM image of the circled area in the insert TEM image. The HRTEM image reveals the polycrystalline nature of Co_3O_4/TiO_2 composite hollow polyhedrons, which are composed of interconnected nanoparticles with a diameter of about several nanometers. The HRTEM image in Figure 4b exhibits lattice fringes with different d-spacings of 4.66 Å, 2.85 Å and 2.33 Å, corresponding to the (111), (220) and (222) planes of cube Co_3O_4 crystals. On the edge of composite hollow polyhedrons, lattice fringes with the d-spacings of 2.37 Å are in good agreement with the interplanar spacings of anatase TiO_2, indicating the formation of TiO_2 grains during thermal treatment.

Electrochemical Performance

To evaluate electrochemical performances of all the samples, coin cells of Co_3O_4/TiO_2 composite hollow polyhedrons and pure Co_3O_4 hollow polyhedrons cycled in a voltage range of 0.01 - 3 V *versus* Li^+/Li. As a novel composite anode material for LIBs, cyclic voltammetry (CV) profile of Co_3O_4/TiO_2 composite hollow polyhedrons is carried out at a scan rate of 0.1 mV/s in a potential region of 0.01 - 3 V to explore the lithium insertion/extraction behaviors. The electrochemical reactions of Co_3O_4 and TiO_2 with lithium are described below:

$$Co_3O_4 + 8Li^+ + 8e^- = 4Li_2O + 3Co \quad (1)$$

$$TiO_2 + xLi^+ + xe^- = LixTiO_2\ (x \leq 1) \quad (2)$$

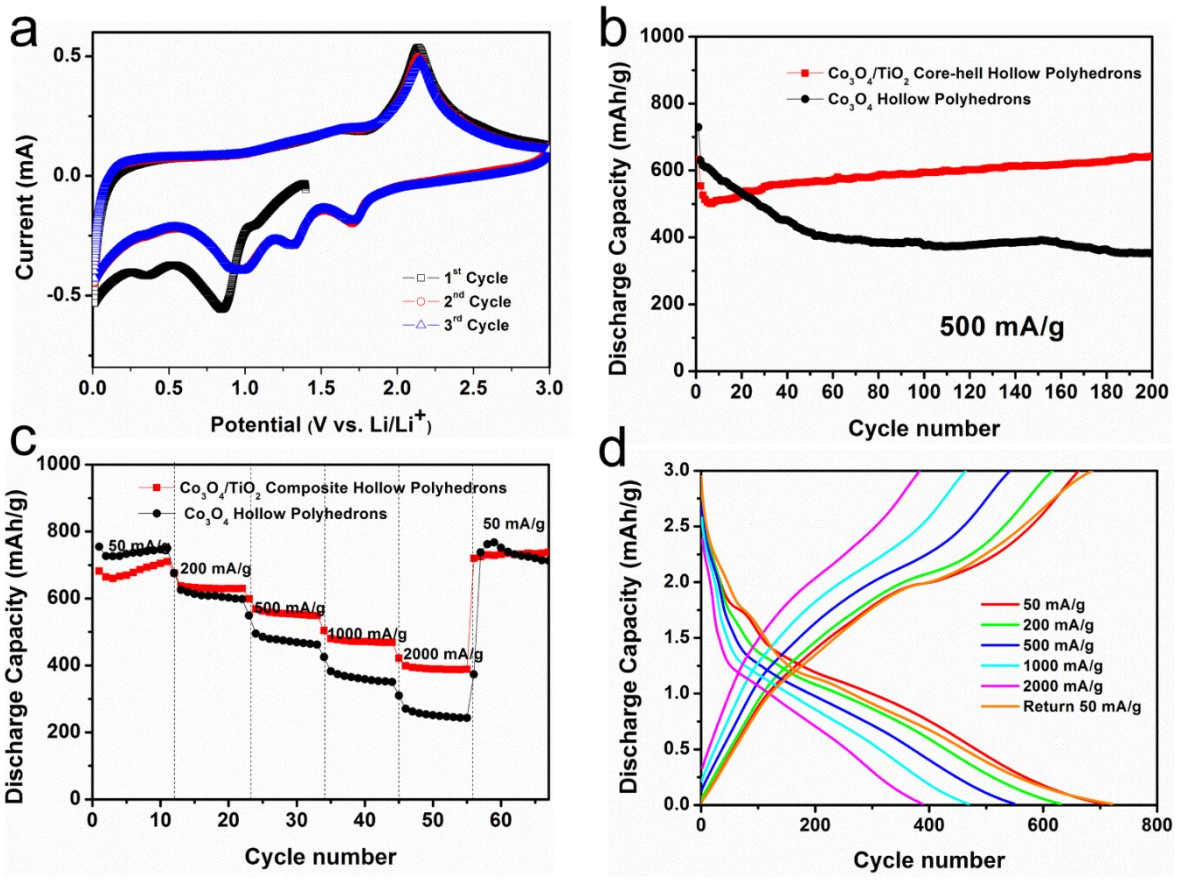

Figure 3-5 (a) CV curves at scan rate of 0.1 mV/s, (b) cycling performance at 500 mA/g, (c) rate performance at the current density range from 100, 500, 1000, 2000, 2000 and 100 mA/g, (d) charge/discharge profiles of corresponding to the rate performance.

Figure 5a displays the CV curves of Co_3O_4/TiO_2 composite hollow polyhedrons. In the first cathodic scan, a small peak at around 1.08 V *vs*. Li/Li^+ is ascribed to the irreversible insertion of lithium ions to form the $Li_xCo_3O_4$ phase. During the continuous discharge process, the prominent potentials at around 0.85 V is observed, corresponding to destruction of crystal structure and formation of solid–electrolyte interphase (SEI) films. During the following anodic scan, a broad peak located at about 2.13 V *vs.* Li/Li^+ is ascribed to the re-oxidization of metallic cobalt and the decomposition of Li_2O according to the reversible conversion mechanism described by the equation (reaction 1). In subsequent cycles, three cathodic peaks and one broad anodic peak can be clearly observed. The characteristic cathodic peak at 1.7 V and anodic peak at 2.0 V are attributed to the lithium intercalation/extraction into/from anatase TiO_2 (reaction 2). The broad anodic peak at 2.13 and two cathodic peaks at 1.3 and 0.9 V are associated with the reversible oxidation/reduction of Co/Co_3O_4 (reaction 1). The anodic peak of TiO_2 at 2.0 V is overlapped by the anodic peak of Co_3O_4, forming a broad peak located at 2.13 V. Figure S5 exhibits the voltage profiles of the Co_3O_4/TiO_2 composite for the first three cycles. The identified charge-discharge platforms are consistent with the result of the CV analysis above. In Figure S5, the broad sloping plateau at 0.8 - 1.1 V may be related to the initial reduction of Co_3O_4 to Co, and the formation of irreversible solid electrolyte interphase (SEI) film. It is observed that the initial discharge and charge capacities of the Co_3O_4/TiO_2 composite are 662 and 535 mAh/g, respectively. The initial

capacity loss of 19 % may be mainly ascribed to the irreversible processes such as electrolyte decomposition, the formation of SEI films and undecomposed Li_2O phase, which are commonly observed for most anode materials. [43-47] Figure 5b compares cycling performances of Co_3O_4/TiO_2 composite hollow polyhedrons and pure Co_3O_4 hollow polyhedrons when cycled at a specific current of 500 mA/g. It is found that Co_3O_4/TiO_2 composite hollow polyhedrons exhibit an unexpected but interesting cycling performance. It is observed that at a specific current of 500 mA/g, the initial discharge capacity of pure Co_3O_4 hollow polyhedrons is 730 mAh/g, higher than that of Co_3O_4/TiO_2 composite hollow polyhedrons (662 mAh/g). Such phenomenon is attributed to the larger theoretical capacity of Co_3O_4 than that of TiO_2. After 200 cycles, Co_3O_4/TiO_2 composite hollow polyhedrons keep a reversible capacity of 642 mAh/g, maintaining 96.9% of the initial capacity, demonstrating a very large discharge capacity and outstanding cycling stability. In contrast, the reversible capacity of pure Co_3O_4 hollow polyhedrons electrode drops rapidly from 730 to 350 mAh/g, corresponding to a very low capacity retention of 44.9%. This serious capacity fading of pure Co_3O_4 hollow polyhedrons may be caused by expansion/contraction during charge/discharge, leading to severe pulverization and delamination from the underlying current collector. Notably, the specific capacity of the Co_3O_4/TiO_2 composite electrode decreases for the initial 10 cycles and then increases in subsequent cycles. For various nanostructured transition metal-oxide electrodes, this phenomenon of the initial increased capacity is widely observed.[45-47] During the charge-discharge process, the decomposition of the electrolyte leads to formation of an electrochemically gel-like polymer layer on the surface of active materials, which can enhance the Li-ion storage capacity through a so called “pseudo-capacitance-type behavior”.[48] Another possible reason is that Co nanoparticles may be formed at the interface of Co_3O_4/TiO_2

due to some irreversible electrochemical reaction and the presence of Co may improve the reversibility of electrochemical reaction of active material, resulting in improved specific capacity.[49] In Figure 5c, the rate performance of the two samples is evaluated at various specific current ranging from 50 to 2000 mA/g. Co_3O_4/TiO_2 composite hollow polyhedrons exhibit a better rate capability than that of pure Co_3O_4 hollow polyhedrons, especially at high rates. They deliver average discharge capacities of 710, 630, 550, 480 and 400 mAh/g at 50, 200, 500, 1000, and 2000 mA/g, respectively. It is clearly observed that even when the specific current is as high as 2000 mA/g, about 390 mAh/g of the capacity is still retained, much higher than pure Co_3O_4 as well as commercial graphite anode. More importantly, when the specific current returns from 2000 mA/g to 50 mA/g, its discharge capacity recovers to 710 mAh/g immediately and maintains a good capacity retention in the following cycles, indicating very good rate capability of the material. Figure 5d displays galvanostatic charge/discharge curves of the Co_3O_4/TiO_2 composite hollow polyhedrons electrode at specific currents of 100, 500, 1000, 2000, 2000 and 100 mA/g, corresponding to the rate performance. The discharge and charge potential plateaus of each cycle are consistent with corresponding CV redox peaks. The high capacity, long cycling life and excellent rate capability of Co_3O_4/TiO_2 composite hollow polyhedrons can be attributed to the stable composite structure and high conductivity.

Moreover, structural integrity after repeated cycling is a major issue in rechargeable lithium batteries. To examine this aspect, the impedance of the electrode is evaluated after 100 electrochemical cycles, and the EIS results are shown in Figure 6a. EIS technology, one of the most powerful tools for studying electrochemical kinetics, can be used to investigate the processes occurring at the electrode/electrolyte interfaces and Li^+ intercalation/de-intercalation within

electrode materials in the battery cells. In the Nyquist plots, R_Ω represents the Ohmic resistance of the battery cell, including electrodes, electrolyte and other cell components. R_{ct} represents the charge transfer resistance. CPE and Z_w are the double layer capacitance and the Warburg impedance, respectively. The Nyquist plots of all the three electrodes are composed of a depressed semicircle in the medium-frequency region followed by a slanted line in the low-frequency region. The charge transfer resistance of Co_3O_4 hollow polyhedrons is around 125 Ω. After being integrated with TiO_2, the resistance is decreased to 100 Ω, indicating faster charge transfer at the electrode /electrolyte interface for Co_3O_4/TiO_2 composite hollow polyhedrons. After 100 electrochemical cycles, the charge-transfer resistance is further decreased to 75 Ω, owing to the formation of cobalt after irreversible reactions. As for the morphology change, SEM images of Co_3O_4/TiO_2 composite hollow polyhedrons after 200 cycles are shown in Figure 6b. It can be seen the electrode retains its original hollow polyhedrons architecture after 200 cycles. Although the repeated lithiation and delithiation of Co_3O_4 can result in large volume change during cycling, the hollow polyhedral shape is well maintained. In comparison with usually observed collapse of Co_3O_4 electrode, Co_3O_4/TiO_2 composite hollow polyhedrons is remarkably stable.

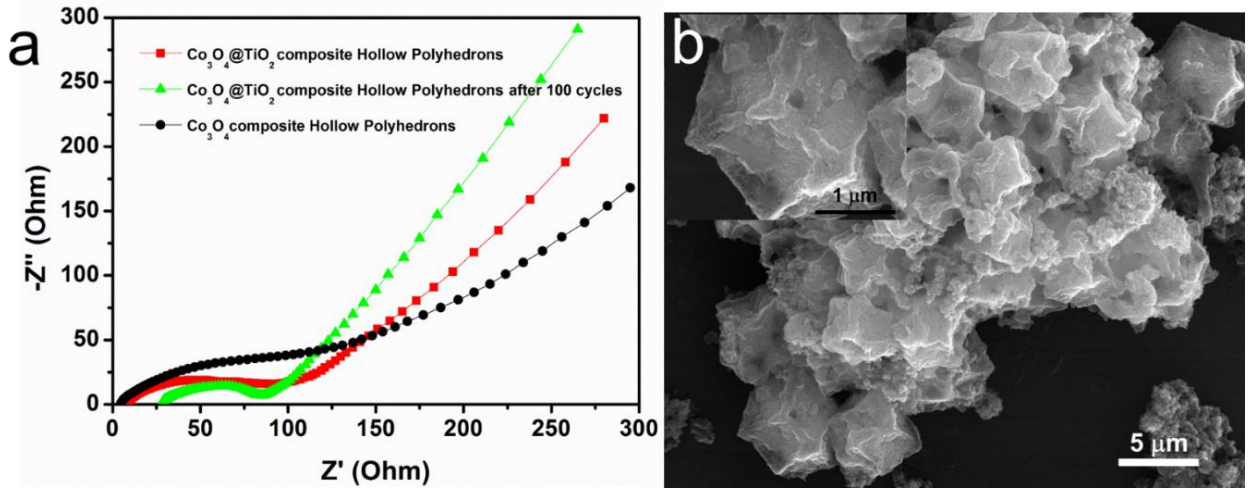

Figure 3-6 (a) Electrochemical impedance spectroscopy of electrodes before and after cycling. (b) SEM of the Co_3O_4/TiO_2 composite hollow polyhedrons after 200 cycles (SEM image of large magnification is inserted).

Finally, the advantages of the novel composite nanostructure electrode are described below. The remarkable performance of the new electrode is attributed to the composite hollow polyhedron structure. First, the uniform integration of titanium ions by cation exchange in ZIF-67, and the simultaneous decomposition and crystallization of TiO_2 contribute the formation of integrated Co_3O_4/TiO_2 composite hollow polyhedrons during sintering. The integration of Co_3O_4/TiO_2 composite promotes the robust stability of hollow polyhedrons nanostructure. Second, the void hollow structure not only facilitates penetration of electrolyte, but also accommodates large volumetric expansion of Co_3O_4 during cycling. Third, the strategy of integration of Co_3O_4 and TiO_2 can realize synergic property of electrochemistry. As a result of these beneficial factors, the Co_3O_4/TiO_2 composite hollow polyhedrons improve the cycling life up to 200 cycles.

3.4 Conclusion

In summary, this report has demonstrated a scalable and controllable approach for fabricating Co_3O_4/TiO_2 composite hollow polyhedrons through a cation-exchange strategy followed by thermal treatment. During the synthesis process, ZIF-67 polyhedrons not only act as a host for the exchanged titanium cations, but also serve as the template for the formation of the hollow framework of Co_3O_4/TiO_2 composite. In such a structure, TiO_2 provides a stable backbone to supply the high capacity of Co_3O_4 durably. In addition, TiO_2 also served as conductive path for higher transportation of electrons. The as-prepared Co_3O_4/TiO_2 composite hollow polyhedrons exhibit long cycling life and remarkable rate capability. At a specific current of 500 mA/g, the

composite nanostructures can provide the initial capacity as high as 662 mAh/g, and maintain a stable capacity of 642 mAh/g after 200 cycles, accounting for 96.9% the initial capacity, much higher than that of pure Co_3O_4 hollow polyhedrons, which can only maintain a specific capacity of 200 mAh/g and a capacity retention of only 40%. Furthermore, the novel cation exchange strategy in this work can be extended to construction of more complex composite nanostructure for broader applications in solar cells, supercapacitor and fuel cells.

3.5 REFERENCES

1. C. Huang, J. Xiao, Y. Shao, J. Zheng, W. D. Bennett, D. P. Lu, L. V. Saraf, M. Engelhard, L. W. Ji, J. W. Zhang, X. L. Li, G. L. Graff, J. Liu, Manipulating surface reactions in lithium-sulphur batteries using hybrid anode structures, Nat. Commun. 5 (2014) 3015.
2. A. Yoshino, The Birth of the Lithium-Ion Battery, Angew. Chem. Int. Ed. 24 (2012) 5798-5800
3. X. F. Wang, X. H. Lu, B. Liu, D. Chen, Y. X. Tong, G. Z. Shen, Flexible Energy-Storage Devices: Design Consideration and Recent Progress, Adv. Mater. 26 (2014) 4763-4782.
4. D. K. Kim, P. Muralidharan, H. W. Lee, R. Ruffo, Y. Yang, C. K. Chan, H. L. Peng, R. A. Huggins, Y. Cui, Spinel $LiMn_2O_4$ nanorods as lithium ion battery cathodes, Nano Lett. 8 (2008) 3948-3952.
5. S. W. Kim, D. H. Seo, X. H. Ma, G. Ceder, K. Kang, Electrode Materials for Rechargeable Sodium Ion Batteries: Potential Alternatives to Current Lithium-Ion Batteries, Adv. Energy Mater. 2 (2012) 710-721.
6. N. Liu, Z. D. Lu, J. Zhao, M. T. McDowell, H. W. Lee, W. T. Zhao, Y. Cui, A PomegranateInspired Nanoscale Design for Large-Volume-Change Lithium Battery Anodes, Nat. Nanotechnol. 9 (2014) 187-192.
7. V. Etacheri, R. Marom, R. Elazari, G. Salitra, D. Aurbach, Challenges in the Development of Advanced Li-ion Batteries: a Review, Energy Environ. Sci. 4 (2011) 3243-3262.

8. W. W. Xu, Z. Q. Xie, X. D. Cui, K. N. Zhao, L. Zhang, G. Dietrich, K. M. Dooley, Y. Wang, Hierarchical Graphene-Encapsulated Hollow SnO_2@ SnS_2 Nanostructures with Enhanced Lithium Storage Capability, ACS Appl. Mater. Interfaces. 7 (2015) 22533- 22541.

9. Q. D. Li, Q. L. Wei, J. Z. Sheng, M. Y. Yan, L. Zhou, W. Luo, R. M. Sun, L. Q. Mai, Mesoporous Li_3VO_4/C Submicro-Ellipsoids Supported on Reduced Graphene Oxide as Practical Anode for Hig-Power Lithiu-Ion Batteries, Adv. Sci. 2 (2015) .

10. Z. Q. Xie, Z. Y. He, X. H. Feng, W. W. Xu, X. D. Cui, J. H. Zhang, C. Yan, M. A. Carreon, Z. Liu, Y. Wang, Hierarchical Sandwich-like Structure of Ultrafine N-Rich Porous Carbon Nanospheres Grown on Graphene Sheets as Superior Lithium-Ion Battery Anodes, ACS Appl. Mater. Interfaces.2016, 8, 10324-10333.

11. Y. Jiang, Z. J. Jiang, B. H. Chen, Z. Q. Jiang, S. Cheng, H. B. Rong, J. L. Huang, M. L. Liu, Morphology and crystal phase evolution induced performance enhancement of MnO2 grown on reduced graphene oxide for lithium ion batteries, J. Mater. Chem. A. 4 (2016) 2643-2650.

12. Q. M. Su, D. Xie, J. Zhang, G. H. Du, B. S. Xu, In Situ Transmission Electron Microscopy Observation of The Conversion Mechanism of Fe_2O_3/Graphene Anode During Lithiation-Delithiation Processes, ACS Nano 7 (2013) 9115-9121.

13. P. Sennu, H. S. Kim, J. Y. An, V. Aravindan, Y. S. Lee, Synthesis of 2D/2D Structured Mesoporous Co_3O_4 Nanosheet/N-Doped Reduced Graphene Oxide Composites as a Highly Stable Negative Electrode for Lithium Battery Applications, Chem. Asian J. 10 (2015) 1776-1783.

14. Z. C. Bai, Z. C. Ju, C. L. Guo, Y. T. Qian, B. Tang, S. L. Xiong, Direct Large-Scale Synthesis of 3D Hierarchical Mesoporous NiO Microspheres as High-Performance Anode Materials for Lithium Ion Batteries, Nanoscale 6 (2014) 3268-3273.

15. P. Meduri, E. Clark, J. H. Kim, E. Dayalan, G. U. Sumanasekera, M. K. Sunkara, MoO_{3-x} Nanowire Arrays as Stable and High-Capacity Anodes for Lithium Ion Batteries, Nano Lett. 12 (2012) 1784-1788.

16. W. W. Xu, K. N. Zhao, C. J. Niu, L. Zhang, Z. Y. Cai, C. H. Han, L. He, T. Shen, M. Y. Yan, L. B. Qu, L. Q. Mai, Heterogeneous Branched Core-Shell SnO_2–PANI Nanorod Arrays with Mechanical Integrity and Three Dimentional Electron Transport for Lithium Batteries, Nano Energy 8 (2014) 196-204.

17. L. Zhang, K. N. Zhao, W. W. Xu, Y. F. Dong, R. Xia, F. N. Liu, L. He, Q. L. Wei, M. Y. Yan, L. Q. Mai. Integrated SnO_2 Nanorod Array with Polypyrrole Coverage for High-Rate and Long-life Lithium Batteries, Phys. Chem. Chem. Phys. 17 (2015) 7619-7623.

18. J. M. Liu, Q. C. Zhang, J. C. Yang, H. Y. Ma, M. O. Tade, S. B. Wang, J. Liu, Facile Synthesis of Carbon-Doped Mesoporous Anatase TiO_2 for The Enhanced Visible-Light Driven Photocatalysis, Chem. Commun. 50 (2014) 13971-13974.

19. X. H. Cao, Y. M. Shi, W. H. Shi, X. H. Rui, Q. Y. Yan, J. Kong, H. Zhang, Preparation of MoS_2-Coated Three-Dimensional Graphene Networks for High-Performance Anode Material in Lithium-Ion Batteries. Small 9 (2013) 3433-3438.

20. B. Luo, Y. Fang, B. Wang, J. S. Zhou, H. H. Song, L. J. Zhi, Two Dimensional Graphene-SnS_2 Hybrids with Superior Rate Capability for Lithium Ion Storage, Energy Environ. Sci. 5 (2012) 5226.

21. H. Hu, L. Han, M. Z. Yu, Z. Y. Wang, X. W. Lou, Metal-Organic-Framework-Engaged Formation of Co Nanoparticle-Embedded Carbon@ Co_9S_8 Double-Shelled Nanocages for Efficient Oxygen Reduction, Energy Environ. Sci. 9 (2016) 107-111.

22. W. Y. Fang, H. B. Zhao, Y. P. Xie, J. H. Fang, J. Q. Xu, Z. W. Chen, Facile Hydrothermal Synthesis of VS_2/Graphene Nanocomposites with Superior High-Rate Capability as Lithium-ion Battery Cathodes, ACS Appl. Mater. Interfaces. 7 (2015) 13044-13052.

23. Y. H. Xu, Q. Liu, Y. J. Zhu, Y. H. Liu, A. Langrock, M. R. Zachariah, C. S. Wang, Nano Lett. 13 (2013) 470-474.

24. Y. J. Hong, M. Y. Son, Y. C. Kang, Uniform Nano-Sn/C Composite Anodes for Lithium Ion Batteries, Adv. Mater. 25 (2013) 2279-2283.

25. Y. J. Zhu, X. G. Han, Y. H. Xu, Y. H. Liu, S. Y. Zheng, K. Xu, L. B. Hu, C. S. Wang, Electrospun Sb/C Fibers for a Stable and Fast Sodium-Ion Battery Anode, ACS Nano 7 (2013) 6378-6386.

26. J. Y. Wang, N. L. Yang, H. J. Tang, Z. H. Dong, Q. Jin, M. Yang, D. Kisailus, H. J. Zhao, Z. Y. Tang, D. Wang. Accurate Control of Multishelled Co_3O_4 Hollow Microspheres as High-Performance Anode Materials in Lithium-Ion Batteries, Angew. Chem. Int. Ed. 125 (2013) 6545-6548.

27. Y. Wang, H. J. Zhang, L. Lu, L. P. Stubbs, C. C. Wong, J. Y. Lin. Designed Functional Systems From Peapod-like Co@ Carbon to Co_3O_4@Carbon Nanocomposites, ACS Nano 4 (2010) 4753-4761.

28. D. Gu, W. Li, F. Wang, H. Bongard, B. Spliethoff, W. Schmidt, C. Weidenthaler, Y. Y. Xia, D. Y. Zhao, F. Schüth, Controllable Synthesis of Mesoporous Peapod-Like Co_3O_4@ Carbon Nanotube Arrays for High-Performance Lithium-Ion Batteries, Angew. Chem. Int. Ed. 54 (2015) 7060-7064.

29. R. W. Mo, Z. Y. Lei, K. N. Sun, D. Rooney. Facile Synthesis of Anatase TiO_2 Quantum-Dot/Graphene-Nanosheet Composites with Enhanced Electrochemical Performance for Lithium-Ion Batteries, Adv. Mater. 26 (2014) 2084-2088.

30. Z. W. Seh, W. Y. Li, J. J. Cha, G. Y. Zheng, Y. Yang, M. T. McDowell, P. C. Hsu, Y. Cui, Sulphur-TiO_2 Yolk-Shell Nanoarchitecture with Internal Void Space for Long-Cycle Lithium-Sulphur Batteries, Nat. Commun. 8 (2013) 1331.

31. Y. S. Luo, J. S. Luo, W. W. Zhou, X. Y. Qi, H. Zhang, D. Y. W. Yu, C. M. Li, H. J. Fan, T. Yu, Controlled Synthesis of Hierarchical Graphene-Wrapped TiO_2@Co_3O_4 Coaxial Nanobelt Arrays for High-Performance Lithium Storage. J. Mater. Chem. A. 1 (2013) 273-281.

32. W. T. Li, K. Shang, Y. M. Liu, Y. F. Zhu, R. H. Zeng, L. Z. Zhao, Y. W. Wu, L. Li, Y. H. Chu, J. H. Liang, G. Liu, A Novel Sandwich-Like Co_3O_4/TiO_2 Composite with Greatly Enhanced Electrochemical Performance as Anode for Lithium Ion Batteries. Electrochim. Acta. 174 (2015) 985-991.

33. H. G. Wang, D. L. Ma, X. L. Huang, Y. Huang, X. B. Zhang, General and Controllable Synthesis Strategy of Metal Oxide/TiO_2 Hierarchical Heterostructures with Improved Lithium-Ion Battery Performance. Sci. Rep. 2 (2012) 701.

34. Y. Q. Fan, N. Zhang, L. Y. Zhang, H. B. Shao, J. M. Wang, J. Q. Zhang, C. N. Cao, Co_3O_4-Coated TiO_2 Nanotube Composites Synthesized Through Photo-Deposition Strategy with Enhanced Performance for Lithium-Ion Batteries. Electrochim. Acta. 94 (2013) 285-293.

35. M. Madian, L. Giebeler, M. Klose, M. Uhlemann, A. Gebert, S. Oswald, N. Ismail, A. Eychmueller, J. Eckert, T. Jaumann, Self-Organized TiO_2/CoO Nanotubes as Potential Anode Materials for Lithium Ion Batteries, *ACS Sustainable Chem. Eng.* 3 (2015) 909-919.

36. C. K. Broze, M. Dinca, Cation Exchange at the Secondary Building Units of Metal-Organic Frameworks, Chem. Soc. Rev. 43 (2014) 5456-5467.

37. A. E. Ringwood, Geochim. Cosmochim. Acta, (7) 1955 189–202.

38. J. An, N. L. Rosi, Tuning MOF CO_2 Adsorption Properties *via* Cation exchange, J. Am. Chem. Soc. 132 (2010) 5578-5579.

39. J. M. Pietryga, D. J. Werder, D. J. Williams, J. L. Casson, R. D. Schaller, V. I. Klimov, J. A. Hollingsworth, Utilizing The Lability of Lead Selenide to Produce Heterostructured Nanocrystals with Bright, Stable Infrared Emission, J. Am. Chem. Soc. 130 (2008) 4879-4885.

40. B. Y. Xia, Y. Yan, N. Li, H. B. Wu, X. W. Lou, X. Wang, A Metal-Organic Framework-Derived Bifunctional Oxygen Electrocatalyst, Nat. Energy 1 (2016) 15006.

41. Z. S. Wu, W. C. Ren, L. Wen, L. B. Gao, J. P. Zhao, Z. P. Chen, G. M. Zhou, F. Li, H. M. Cheng, Co_3O_4 Nanocages for High-Performance Anode Material in Lithium-Ion BatteriesJ. Phys. Chem. C. 116 (2012) 7227.

42. R. Hao, B. J. Jiang, M. X. Li, Y. Xie, H. G. Fu, Fabrication of Mixed-Crystalline-Phase Spindle-Like TiO_2 for Enhanced Photocatalytic Hydrogen Production, Sci. China Mater. 58 (2015) 363-369

43. N. Du, H. Zhang, B. D. Chen, J. B. Wu, X. Y. Ma, Z. H. Liu, Y. Q. Zhang, D. R. Yang, X. H. Huang, J. P. Tu, Porous Co_3O_4 Nanotubes Derived From $Co_4(CO)_{12}$ Clusters on Carbon Nanotube Templates: A Highly Efficient Material For Li-Battery Applications. Adv. Mater. 19 (2007) 4505-4509.

44. L. Tian, H. L. Zou, J. X. Fu, X. F. Yang, Y. Wang, H. L. Guo, X. H. Fu, C. L. Liang, M. M. Wu, P. K. Shen, Q. M. Gao, Topotactic Conversion Route to Mesoporous Quasi-Single-Crystalline Co_3O_4 Nanobelts with Optimizable Electrochemical Performance. Adv. Funct. Mater. 20 (2010) 617-623.

45. Z. Y. Cai, L. Xu, M. Y. Yan, C. H. Han, L. He, K. M. Hercule, C. J. Niu, Z. F. Yuan, W. W. Xu, L. B. Qu, K. N. Zhao, Manganese Oxide/Carbon Yolk-Shell Nanorod Anodes for High Capacity Lithium Batteries. Nano Lett. 15 (2014) 738-744.

46. S. Grugeon, S. Laruelle, L. Dupont, J. M. Tarascon, An Update on the Reactivity of Nanoparticles Co-based Compounds Towards Li. Solid State Sci. 5 (2003) 895-904.

47. Y. M. Sun, X. L. Hu, W. Luo, F. F. Xia, Y. H. Huang, Reconstruction of Conformal Nanoscale MnO on Graphene as a High-Capacity and Long-Life Anode Material for Lithium Ion Batteries. Adv. Funct. Mater. 23 (2013) 2436-2444.

48. S. Laruelle, S. Grugeon, P. Poizot, M. Dolle, L. Dupont and J. M. Tarascon. On the Origin of the Extra Electrochemical Capacity Displayed by MO/Li Cells at Low Potential. J. Electrochem. Soc. 149 (2002) A627-A634.

49. J. S. Luo, X. H. Xia, Y. S. Luo, C. Guan, J. L. Liu, X. Y. Qi, C. F. Ng, T. Yu, H. Zhang, H. J. Fan, Rationally Designed Hierarchical TiO_2@ Fe_2O_3 Hollow Nanostructures for Improved Lithium Ion Storage. Adv. Energy Mater. 3 (2013) 737-743

CHAPTER 4. CONCLUSIONS

In this thesis, two strategies have been developed to improve the electrochemical performance of anode materials for lithium ion batteries. The 1st strategy is to design hierarchical graphene-encapsulated hollow SnO_2@SnS_2 nanostructures by in-situ sulfuration on the backbones of hollow SnO_2 spheres via a simple hydrothermal method followed by a solvothermal surface modification. The as-prepared hierarchical SnO_2@SnS_2@rGO nanocomposite can be used as anode material in lithium ion batteries, exhibiting excellent cycleability with a capacity of 583 mAh/g after 100 electrochemical cycles at a specific current of 200 mA/g. This material shows a very low capacity fading of only 0.273% per cycle from the 2nd to the 100th cycle, lower than the capacity degradation of bare SnO_2 hollow spheres (0.830%) and single SnS_2 nanosheets (0.393%). Even after being cycled at a range of specific current varied from 2000 mA/g to 100 mA/g, hierarchical SnO_2@SnS_2@rGO nanocomposite maintains a reversible capacity of 664 mAh/g, which is much higher than single SnS_2 nanosheets (374 mAh/g) and bare SnO_2 hollow spheres (177 mAh/g). Such significantly improved electrochemical performance can be attributed to the unique hierarchical hollow structure, which not only effectively alleviates the stress resulted from the lithiation/delithiation process and maintains structural stability during cycling but also reduces aggregation and facilitates ion transportation. This work thus demonstrates the great potential of hierarchical SnO_2@SnS_2@rGO nanocomposites for application as high-performance anode material in next-generation lithium ion battery technology. The 2nd strategy is to fabricate integrated Co_3O_4/TiO_2 composite hollow polyhedrons through a cation-exchange approach in metal-organic framework. In this synthesis, well-defined ZIF-67 particles not only serve as the host to accommodate exchanged titanium cations but also the template to form hollow polyhedron structure. The obtained integrated Co_3O_4/TiO_2 composite hollow polyhedrons exhibit a high reversible capacity of 642 mAh/g at a rate of 500 mA/g after 200 cycles, accounting for 96.9% of the initial capacity, much higher than that of pure Co_3O_4, which only maintain a specific capacity of 200 mAh/g and a capacity retention of 40%. The optimized integrated Co_3O_4/TiO_2 composite hollow polyhedrons display significant improvements in electrochemical performance, demonstrating great potential as advanced anode material for future lithium ion batteries.

PERMISSION TO USE COPYRIGHTED MATERIALS

6/23/2017 Rightslink® by Copyright Clearance Center

Copyright Clearance Center RightsLink®

Home | Account Info | Help

ACS Publications Most Trusted. Most Cited. Most Read.

Title: Hierarchical Graphene-Encapsulated Hollow SnO2@SnS2 Nanostructures with Enhanced Lithium Storage Capability

Author: Wangwang Xu, Zhiqiang Xie, Xiaodan Cui, et al

Publication: Applied Materials

Publisher: American Chemical Society

Date: Oct 1, 2015

Copyright © 2015, American Chemical Society

Logged in as: Wangwang Xu
Account #: 3001165974
LOGOUT

PERMISSION/LICENSE IS GRANTED FOR YOUR ORDER AT NO CHARGE

This type of permission/license, instead of the standard Terms & Conditions, is sent to you because no fee is being charged for your order. Please note the following:

- Permission is granted for your request in both print and electronic formats, and translations.
- If figures and/or tables were requested, they may be adapted or used in part.
- Please print this page for your records and send a copy of it to your publisher/graduate school.
- Appropriate credit for the requested material should be given as follows: "Reprinted (adapted) with permission from (COMPLETE REFERENCE CITATION). Copyright (YEAR) American Chemical Society." Insert appropriate information in place of the capitalized words.
- One-time permission is granted only for the use specified in your request. No additional uses are granted (such as derivative works or other editions). For any other uses, please submit a new request.

BACK | CLOSE WINDOW

ELSEVIER LICENSE
TERMS AND CONDITIONS

Jun 23, 20

This Agreement between Wangwang Xu ("You") and Elsevier ("Elsevier") consists of your license details and the terms and conditions provided by Elsevier and Copyright Clearance Center.

License Number	4134850976240
License date	Jun 23, 2017
Licensed Content Publisher	Elsevier
Licensed Content Publication	Electrochimica Acta
Licensed Content Title	Integrated Co3O4/TiO2 Composite Hollow Polyhedrons Prepared via Cation-exchange Metal-Organic Framework for Superior Lithium-ion Batteries
Licensed Content Author	Wangwang Xu,Xiaodan Cui,Zhiqiang Xie,Grant Dietrich,Ying Wang
Licensed Content Date	Dec 20, 2016
Licensed Content Volume	222
Licensed Content Issue	n/a
Licensed Content Pages	8
Start Page	1021
End Page	1028
Type of Use	reuse in a thesis/dissertation
Portion	full article
Format	both print and electronic
Are you the author of this Elsevier article?	Yes
Will you be translating?	No
Order reference number	
Title of your thesis/dissertation	NOVEL DESIGN OF NANOSTRUCTURED MATERALS FOR ADVANCED ENERGY CONVERSION AND STORAGE DEVICES
Expected completion date	Aug 2017
Estimated size (number of pages)	70
Elsevier VAT number	GB 494 6272 12
Requestor Location	Wangwang Xu 1717 S Brightside View DR, APT A BATON ROUGE, LA 70820

VITA

Wangwang Xu obtained his Bachelor's degree in 2012 and Master's degree in 2014 from Wuhan University of Technology. He is currently a Ph.D. student in the Mechanical & Industrial Engineering Department at Louisiana State University under the supervision of Dr. Ying Wang. His research interests are in the development of advanced materials for lithium-ion batteries and supercapacitors. Wangwang Xu's professional publications in master program at LSU are listed as follows:

1. W. W. Xu, Z. Q. Xie, X. D. Cui, K. N. Zhao, L. Zhang, G. Dietrich, K. M. Dooley, Y. Wang; Hierarchical Graphene-Encapsulated Hollow SnO_2@SnS_2 Nanostructures with Enhanced Lithium Storage Capability, *ACS applied materials & interfaces*. 2015, 7, 22533-22541.
2. W. W. Xu, X. D. Cui, Z. Q. Xie, G. Dietrich, Y. Wang; Integrated Co_3O_4/TiO_2 Composite Hollow Polyhedrons Prepared via Cation-exchange Metal-Organic Framework for Superior Lithium-ion Batteries. *Electrochimica Acta*. 2016, 222, 1021-1028.